Correlation density matrices for one-dimensional quantum chains based on the density matrix renormalization group

2010 New J. Phys. 12 075027

(http://iopscience.iop.org/1367-2630/12/7/075027)

New Journal of Physics
The open-access journal for physics

Correlation density matrices for one-dimensional quantum chains based on the density matrix renormalization group

W Münder[1,3], A Weichselbaum[1], A Holzner[1], Jan von Delft[1] and C L Henley[2]

[1] Physics Department, Arnold Sommerfeld Center for Theoretical Physics and Center for NanoScience, Ludwig-Maximilians-Universität, 80333 Munich, Germany
[2] Laboratory of Atomic and Solid State Physics, Cornell University, Ithaca, NY, 14853-2501, USA
E-mail: wolfgang.muender@physik.uni-muenchen.de

New Journal of Physics **12** (2010) 075027 (50pp)
Received 4 February 2010
Published 28 July 2010
Online at http://www.njp.org/
doi:10.1088/1367-2630/12/7/075027

Abstract. A useful concept for finding numerically the dominant correlations of a given ground state in an interacting quantum lattice system in an unbiased way is the correlation density matrix (CDM). For two disjoint, separated clusters, it is defined to be the density matrix of their union minus the direct product of their individual density matrices and contains all the correlations between the two clusters. We show how to extract from the CDM a survey of the relative strengths of the system's correlations in different symmetry sectors and the nature of their decay with distance (power law or exponential), as well as detailed information on the operators carrying long-range correlations and the spatial dependence of their correlation functions. To achieve this goal, we introduce a new method of analysing the CDM, termed the dominant operator basis (DOB) method, which identifies in an unbiased fashion a small set of operators for each cluster that serve as a basis for the dominant correlations of the system. We illustrate this method by analysing the CDM for a spinless extended Hubbard model that features a competition between charge density correlations and pairing correlations, and show that the DOB method successfully identifies their relative strengths and dominant correlators. To calculate the ground state of

[3] Author to whom any correspondence should be addressed.

this model, we use the density matrix renormalization group, formulated in terms of a variational matrix product state (MPS) approach within which subsequent determination of the CDM is very straightforward. In an extended appendix, we give a detailed tutorial introduction to our variational MPS approach for ground state calculations for one-dimensional quantum chain models. We present in detail how MPSs overcome the problem of large Hilbert space dimensions in these models and describe all the techniques needed for handling them in practice.

Contents

1. Introduction **3**
2. Goals of the DOB method **4**
3. Model **6**
3.1. Definition of the model . . . 6
3.2. Expectations for simple limiting cases . . . 7
3.3. Smooth boundary conditions . . . 8
4. Calculation of the CDM **8**
4.1. Definition of the CDM . . . 8
4.2. DMRG calculation of the CDM . . . 9
4.3. Symmetry sectors . . . 10
4.4. 'Restoration' of numerically broken symmetries . . . 10
5. Finding a distance-independent DOB **11**
5.1. Need for operator bases for clusters A and B . . . 11
5.2. Construction of the DOB . . . 12
5.3. Definition of f-matrix . . . 13
5.4. Fourier analysis and decay of f-matrix . . . 14
6. Numerical results: general remarks **15**
6.1. Specification of clusters A and B . . . 15
6.2. Average site occupation . . . 16
6.3. Rms net correlations $w_{\Delta N}(r)$ . . . 17
7. Numerical results: symmetry sectors **18**
7.1. Charge-density correlations . . . 18
7.2. One-particle correlations . . . 23
7.3. Two-particle correlations . . . 26
8. Comparison to previous results **27**
9. Conclusions **30**
10. Outlook: larger cluster sizes **31**
Acknowledgments **31**
Appendix. The variational MPS approach **32**
References **50**

1. Introduction

In an interacting quantum lattice model, the ground state may have several kinds of correlations, such as long-range order, power-law or exponentially decaying correlations. In the numerical treatment of such a model, it is not clear *a priori* what kind of correlation will be dominant and what kind of operators corresponds to these correlations. Before calculating correlation functions, one typically chooses in advance which operators to consider, using prior knowledge and making initial assumptions. The need to make such choices introduces a certain bias into the investigation, which can be somewhat unsatisfying, especially when hidden or exotic correlations are present.

The correlation density matrix (CDM) has been proposed by Cheong and Henley [1] as an unbiased tool to discover the dominant kind of correlations between two separated clusters, given the density matrix for their union (obtained by tracing out the rest of the system). For two disjoint, separated clusters A and B the CDM is defined to be the density matrix of their union minus the direct product of their respective density matrices to get rid of trivial correlations,

$$\hat{\rho}^C \equiv \hat{\rho}^{A\cup B} - \hat{\rho}^A \otimes \hat{\rho}^B, \tag{1.1}$$

which is completely unbiased except for the specification of the clusters. If the two clusters were not correlated at all, this would imply $\hat{\rho}^{AB} = \hat{\rho}^A \otimes \hat{\rho}^B$ and therefore $\hat{\rho}^C = 0$. The CDM encodes all possible correlations between clusters A and B, as can be seen from the fact that

$$\begin{aligned}\mathrm{tr}(\hat{\rho}^C \hat{O}^A \otimes \hat{O}'^B) &= \mathrm{tr}(\hat{\rho}^{A\cup B}(\hat{O}^A \otimes \hat{O}'^B)) - \mathrm{tr}((\hat{\rho}^A \hat{O}^A) \otimes (\hat{\rho}^B \hat{O}'^B)) \\ &= \langle \hat{O}^A \hat{O}'^B \rangle - \langle \hat{O}^A \rangle \langle \hat{O}'^B \rangle \equiv C_{\hat{O}\hat{O}'},\end{aligned} \tag{1.2}$$

where $\hat{O}^A$ and $\hat{O}'^B$ are operators acting on clusters A and B, respectively.

The very fact that the CDM encodes all possible correlations between two clusters also implies that it is a rather complex, unwieldy object. Indeed, if clusters A and B each have n sites and the local Hilbert space per site is d, the CDM can be represented as a matrix with d^{4n} elements. Moreover, this matrix will typically be calculated as a function of separation r between the clusters. Thus, even if the CDM is already known (e.g. via a highly accurate method for calculating ground states, such as DMRG), it is a highly nontrivial challenge to extract useful, easily digestible information from the mass of data that constitutes the CDM.

The goal of this paper is to propose a systematic method for meeting this challenge. It will be referred to as the dominant operator basis (DOB) method below. The DOB method extracts from the CDM only the dominant correlations of the model, does so in an unbiased fashion and efficiently truncates all information pertaining to correlations of negligible weight. In particular, the DOB method produces a short (!) list of operators per cluster that carry the dominant correlations, together with the set of their mutual correlation functions. This list constitutes the model's DOB (hence the method's proposed name). It turns out that it is possible to formulate the DOB method rather succinctly in general, abstract terms: we do so in the space of just more than three pages, in section 5, which constitutes the heart of this paper and presents its central conceptual advances. Moreover, the general formulation of the DOB method does not depend on cluster size; although in this paper 'cluster' refers to a small number of contiguous sites and we have tried and tested the method only for small clusters, we formulate the method in full generality for clusters of arbitrary size.

To illustrate how the DOB method works in practice, we have chosen to apply it to a certain extended Hubbard model, due to Cheong and Henley [2], involving correlated hopping of

spinless fermions on a two-leg chain. We have two main reasons for this particular choice: firstly, the model shows a rather nontrivial competition between charge density (CD) correlations and pairing correlations, providing a challenging test for a method designed to discover a model's dominant correlations without prior information. Secondly, exact results on this model are available in various limiting regions of parameter space, obtained in [2] using nontrivial mappings to hardcore bosons and free fermions. This information serves as a useful consistency check for the results of our numerical analysis. We would like to emphasize, however that it is *not* our purpose to analyse this model in comprehensive detail (indeed, we study only one particular regime of its large parameter space), nor to calculate its dominant correlation functions with very high accuracy (e.g. to determine the exponents characterizing power-law decays with very small error bars). While the DOB is certainly capable of producing such information (the only prerequisite is that the CDM that is fed into the DOB method needs to be calculated with sufficient accuracy), such a study is beyond the scope of the present work and is left for a separate investigation. Instead, since our interest here is primarily in methodology, we will be content to use this model as a vehicle for illustrating the DOB method in action.

The CDM in [1] was calculated using the full ground state obtained from exact diagonalization. This limits the system size, so that the method was appropriate mainly in cases of rapidly decaying or non-decaying correlations—not for critical or slowly decaying ones. In the present work, we use the density matrix renormalization group (DMRG) [3, 4] (see the excellent review by Schollwöck [5]) to compute the ground state for a ladder system that is known to have algebraic correlations [2]. We use the matrix product state (MPS) formulation of DMRG [6] in which an efficient variational procedure is used to obtain the ground state.

The structure of the main body of the paper is as follows: in section 2, we outline the ideas behind the DOB method in general terms. In section 3, we introduce the model to be considered for explicit calculations. In section 4, we show how the CDM is defined, how to calculate it and explain how a first survey of the relative strengths of various types of correlations can be obtained. In section 5, we give a detailed exposition of the DOB method for constructing a DOB. Sections 6–8 present our numerical results. Our conclusions are given in section 9 and an outlook in section 10. In an extended appendix, we offer a tutorial introduction to the MPS formulation of DMRG and also explain how it can be used to efficiently calculate the CDM.

2. Goals of the DOB method

To extract useful information from the CDM, it will be helpful to develop some intuition of its general structure. To this end, let us recall some fundamental facts from one-dimensional critical fermion systems. They are described by the Luttinger liquid theory, in which one of the key parameters is the Fermi wave vector k_F. The asymptotic behaviour of any kind of correlation or Green's function is typically an oscillation inside a power-law envelope,

$$C(r) \sim \cos(mk_F r + \phi)/r^{\gamma}, \tag{2.1}$$

for some exponent γ, where m is some integer. For the particular model to be used in this study, a nontrivial mapping is known to a free fermion chain [2], a special case of a Luttinger liquid.

The renormalization group theory [7] quite generally implies the existence of *scaling operators* in any critical system such as a Luttinger liquid. They are eigenvectors of the renormalization transformation and, consequently, their correlations are purely of a form like (2.1) for all r, not just asymptotically. The scaling operators usually have complicated forms.

The correlation of a simple operator (e.g. fermion density $n(x)$ at position x along a chain) has overlap with various scaling operators, and correspondingly the correlation function of that simple operator is a linear combination of contributions like (2.1) from those scaling operators.

Our aim is to discover the leading scaling operators numerically. The leading scaling operator encodes all the local fluctuations that are correlated with faraway parts of the system. Intuitively, for a given cluster A, that operator does not depend significantly on the exact position of the (distant) cluster B. That is particularly obvious in a one-dimensional system: any correlation at distances $r' > r$ must be propagated through some sort of correlation at r, so we expect the same operators from cluster A to be involved in $\hat{\rho}^C(r)$, irrespective of the distance r.

This suggests an ansatz for leading contributions in the CDM:

$$\hat{\rho}^C(r) = \sum_s \hat{O}^{A,s} \otimes \hat{O}^{B,s} c_s \frac{e^{ik_s r}}{r^{\gamma_s}}. \tag{2.2}$$

Here $\hat{O}^{A,s}$ and $\hat{O}^{B,s}$ are a pair of (distance-independent) scaling operators acting on clusters A and B, respectively, k_s is the characteristic wave vector for oscillations in their correlation, and γ_s is the corresponding scaling exponent. When $k_s \neq 0$, the operator pairs must themselves come in pairs, labelled, say, by s and $s+1$, with $k_{s+1} = -k_s$, $c_{s+1} = c_s^*$, and $\gamma_{s+1} = \gamma_s$, so that $\hat{\rho}^C$ is Hermitian. The scaling operators for each cluster form an orthonormal set. We expect that only a few terms in the sum in (2.2) capture most of the weight. Correspondingly, it may be feasible to truncate the complete basis sets $\hat{O}^{A,s}$ and $\hat{O}^{B,s}$ to a smaller set of 'dominant operators', whose correlators carry the dominant correlations of the system. The ansatz (2.2) will guide our steps in the ensuing analysis; at the end, we shall check how well it is satisfied by the actual CDMs calculated for the model studied in this paper (see section 7.1.2).

Note that although a particular correlation function may have nodes, see (2.1), for a CDM of the form (2.2) the norm

$$\|\hat{\rho}^C(r)\|^2 = \sum_s \frac{|c_s|^2}{r^{2\gamma_s}} \tag{2.3}$$

is monotonically decaying with r. This expresses the fact that information can only be lost with increasing distance, never restored, in a one-dimensional system.

In [1], the operators entering the dominant correlation were found by a kind of singular value decomposition (SVD), which was done independently for each separation. However, the operators obtained from the SVD will in general be different for different separations r. This does not correspond to the form (2.2), where the operators are distance independent and only the coefficients are r dependent. Therefore, we shall explore in this paper a new scheme to decompose the CDMs for all separations in concert, so as to obtain a small set of scaling operators characterizing the dominant correlations at any (sufficiently large) separation. We decompose $\hat{\rho}^C$ in the form

$$\hat{\rho}^C(r) = \sum_{S_i} \left(\sum_{\mu\mu'} f^{\mu,\mu'}(r) \hat{O}^{A,\mu} \otimes \hat{O}^{B,\mu'} \right)_{S_i}, \tag{2.4}$$

where the S_i represent the symmetry sectors of the discrete, Abelian symmetries of the Hamiltonian (see section 4.3). The subscript of the brackets indicates that the decomposition within the brackets is done for each symmetry sector individually. This decomposition is

possible for any two complete, r-independent operator sets $\hat{O}^{A,\mu}$ and $\hat{O}^{B,\mu'}$ acting on the part of the Hilbert space of clusters A and B, respectively, which correspond to the symmetry sector S_i. The goal is to find two operator sets $\hat{O}^{A,\mu}$ and $\hat{O}^{B,\mu'}$ such that these operator sets may be truncated to a small number of operators each, while still bearing the dominant correlations of the system. These truncated sets of operators will constitute the desired DOBs for the two clusters. The distance dependence of the CDM is then only contained in the matrix $f^{\mu,\mu'}(r)$. Then, all the analysis concerning the distance-dependence of correlations can be done in terms of this f-matrix.

3. Model

To be concrete in the following analysis of the CDM, we begin by introducing the model for which we did our numerical calculations. This model contains rich physics and its treatment below can readily be generalized to other models.

3.1. Definition of the model

We analyse the CDM for a class of spinless extended Hubbard models for fermions, which was intensely studied by Cheong and Henley [2]. They computed correlation functions up to separations of about $r = 20$, using nontrivial mappings to free fermions and hardcore bosons. The correlation functions are calculated with an intervening-particle expansion [2], which expresses the correlation functions in terms of one-dimensional Fermi-sea expectation values (an evaluation of the CDM for that model has also been done by Cheong and Henley [1], using exact diagonalization, but the system sizes are too short to be conclusive). For spinless fermions on a two-leg ladder with length N, we use the following Hamiltonian:

$$\begin{aligned} H = & -t_{\parallel} \sum_{a=1}^{2} \sum_{x=1}^{N-1} (\hat{c}_{a,x}^{\dagger} \hat{c}_{a,x+1} + \text{h.c.}) - t_{\perp} \sum_{x=1}^{N} (\hat{c}_{1,x}^{\dagger} \hat{c}_{2,x} + \text{h.c.}) \\ & - t_{\text{c}} \sum_{x=2}^{N-1} (\hat{c}_{1,x-1}^{\dagger} \hat{n}_{2,x} \hat{c}_{1,x+1} + \hat{c}_{2,x-1}^{\dagger} \hat{n}_{1,x} \hat{c}_{2,x+1} + \text{h.c.}) \\ & + V \sum_{a=1}^{2} \sum_{x=1}^{N-1} \hat{n}_{a,x} \hat{n}_{a,x+1} + V \sum_{x=1}^{N} \hat{n}_{1,x} \hat{n}_{2,x}, \end{aligned} \tag{3.1}$$

where $\hat{c}_{a,x}$ destroys a spinless fermion on leg a and rung x and $\hat{n}_{a,x} = \hat{c}_{a,x}^{\dagger} \hat{c}_{a,x}$ is the corresponding number operator. Effectively, the model corresponds to a one-dimensional pseudo-spin chain, where the $a = 1$ leg is denoted by spin $\uparrow$ and the $a = 2$ leg by spin $\downarrow$. Hence, in the following sections, which generally apply to quantum chain models, we will treat this model as a quantum chain consisting of N sites and return to view the system as a ladder model in the sections where we discuss our results. We define the filling ν to be the average number of particles per site (see equation (3.2) below).

We will focus on infinite nearest-neighbour repulsion $V \to \infty$, which we implement differently along the legs and the rungs in our numerical calculations. In the pseudo-spin description, we can enforce the nearest-neighbour exclusion along the rungs by removing double occupancy from the local Hilbert space of the pseudo-spin sites. The nearest-neighbour

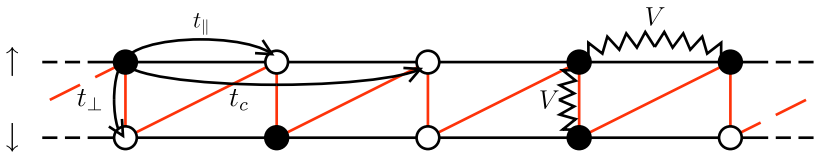

Figure 1. Ladder model with the terms of the Hamiltonian in (3.1). Fermions are depicted by black circles and empty lattice positions by white circles. The ordering used for our Jordan–Wigner transformation of fermionic creation and annihilation operators is depicted by the red line.

exclusion along the legs cannot be implemented so easily and we mimic $V \to \infty$ by a value of V that is much larger than all the other energies in the Hamiltonian (typically $V/t_\parallel = 10^4$).

For fermionic systems, the fermionic sign due to the anti-commutation relations of the fermionic creation and annihilation operators needs to be taken into account. Specifically, we have to choose an order in which we pick the Fock basis, where we have to keep in mind that this choice produces a so-called Jordan–Wigner string of the form $\sum_{x''=x+1}^{x'-1} \mathrm{e}^{\mathrm{i}\pi\hat{n}_{x''}}$ when evaluating correlators $\langle \hat{c}_x \hat{c}^\dagger_{x'} \rangle$ at distance $r = |x - x'|$. In the present system, it is convenient to choose this order such that the operators of the two sites of a rung are succeeding each other (see figure 1), as this choice yields the shortest Jordan–Wigner strings.

3.2. Expectations for simple limiting cases

Setting $t_\parallel \equiv 1$ as a reference scale, we are left with two parameters in the Hamiltonian: the rung hopping $t_\perp$ and the correlated hopping t_c. The physics of the system is governed by the competition of $t_\perp$ to localize the fermions on the rungs and t_c to pair the fermions. There are three limiting cases that have been studied in detail by Cheong and Henley [1, 2].

(i) The paired limit, $t_c \gg t_\parallel, t_\perp$ (we used $t_c/t_\parallel = 10^2$ and $t_\perp = 0$ for our calculations). In this limit, the fermions form tight pairs that behave similarly to hardcore bosons [2]. For two given rungs x and $x+1$, there are two possibilities to create a pair of fermions, due to infinite nearest-neighbour repulsion: $\hat{c}^\dagger_{\uparrow x}\hat{c}^\dagger_{\downarrow x+1}$ and $\hat{c}^\dagger_{\downarrow x}\hat{c}^\dagger_{\uparrow x+1}$. It has been shown in [2] that, based on these two bound pairs, one may classify the bound pairs in two flavours along the ladder and that the ground state has only one definite flavour, causing a twofold symmetry breaking in the ground state. This symmetry breaking introduces complications that will be addressed below. The dominant correlations are expected to be charge-density correlations at short distances and two-particle correlations at long distances. These charge-density and two-particle correlations decay as power laws, oscillating with $k = 2k_\mathrm{F}$, where the Fermi wavelength k_F is related to the filling as $k_\mathrm{F} = \pi\nu$ [2]. In this system, the one-particle correlations are suppressed and are expected to decay exponentially, as a nonzero expectation value depends on a local fluctuation completely filling the rungs between the clusters (as elaborated in section 7.2).

(ii) The two-leg limit, $t_\perp \ll t_\parallel$, $t_c = 0$. In this limit, the two legs are decoupled with respect to hopping, but still the infinite nearest-neighbour repulsion introduces correlations between the two legs. At large distances, power-law charge-density correlations dominate, while

two-particle correlations show much faster power-law decay and one-particle correlations decay exponentially.

(iii) The rung-fermion limit, $t_\perp \gg t_\parallel$, $t_c = 0$. In this limit, the particles are delocalized along the rungs. For fillings smaller than quarter filling, charge-density, one-particle and two-particle correlations all decay as power laws where charge-density correlations dominate at large distances.

Our analysis in this paper is limited to case (i), where DMRG also showed the best performance.

3.3. Smooth boundary conditions

For a ladder of length N (treated as a pseudo-spin chain), we have attempted to reduce effects from the boundaries by implementing *smooth boundary conditions*, adapting a strategy proposed in [8] for a spin chain to our present fermionic system. (Alternatively, it is possible to use periodic boundary conditions [6]. However, this leads to some difficulties, since it is not possible to work with orthonormal basis sets describing the left or right part of the chain with respect to a given site.) Smooth boundary conditions are open boundary conditions together with an artificial decay of all terms of the Hamiltonian over the last M rungs at each end of the chain. We shall calculate expectation values only of operators located in the central part of the system (sites x, with $M < x \leqslant N - M$); thus the system's effective length is $N' = N - 2M$. For the numerical results presented in this paper, we choose the following combinations of chain length and boundary size: $(N, M) = (100, 20)$, $(150, 30)$ and $(200, 40)$.

For both smooth and open boundary conditions, the average site filling strongly decreases near the boundaries. To determine the average filling ν, which influences the system's correlations in an important manner, we thus use only the central N' sites:

$$\nu = \sum_{x=M+1}^{N-M} \left(\langle \hat{n}_{\uparrow x}\rangle + \langle \hat{n}_{\downarrow x}\rangle\right)/(2N') \,. \tag{3.2}$$

Due to the infinite nearest-neighbour repulsion, this implies that $\nu \in [0, 0.5]$.

4. Calculation of the CDM

Throughout the paper we will use the Frobenius inner product and norm for any matrices M_{ij} and M'_{ij} of matching dimension,

$$\langle M, M'\rangle \equiv \sum_{ij} M^*_{ij} M'_{ij} = \mathrm{tr}(M^\dagger M'), \tag{4.1}$$

$$\|M\| \equiv \langle M, M\rangle^{1/2}. \tag{4.2}$$

4.1. Definition of the CDM

We take two disjoint, separated clusters A and B of equal size from a one-dimensional quantum chain, i.e. two sets of adjacent sites $x^A_1, \ldots, x^A_n$ and $x^B_1, \ldots, x^B_n$, where n is the size of the clusters and all the indices x are distinct from each other. In the present study, both clusters will comprise only two rungs, i.e. they support only 'local' operators. While the formulation of the DOB method is independent of cluster size, the version presented here has been tailored to

situations where the cluster used is the smallest possible one consistent with the symmetries of the important operators. We have not tested its performance for larger clusters.

The local Hilbert spaces of clusters A and B with dimension d^n are described in terms of sets of basis states $|\alpha\rangle$ and $|\beta\rangle$, which are product states of the local states of each site in the cluster. The CDM of the two clusters, defined by (1.1), can be expanded in this basis as

$$\hat{\rho}^C = \rho^C_{\alpha\beta\alpha'\beta'}|\alpha\rangle|\beta\rangle\langle\alpha'|\langle\beta'|. \tag{4.3}$$

For processing the CDM we fuse the two indices of each cluster [1]:

$$\tilde{\rho}^C_{\tilde{\alpha}\tilde{\beta}} \equiv \tilde{\rho}^C_{(\alpha\alpha')(\beta\beta')}|\alpha\rangle\langle\alpha'||\beta\rangle\langle\beta'| \tag{4.4}$$

with $\tilde{\alpha} = (\alpha\alpha')$ and $\tilde{\beta} = (\beta\beta')$, and denote the reshaped object $\tilde{\rho}^C$ itself by an extra tilde. This corresponds to a partial transpose of the CDM (note that $\tilde{\rho}^C$ is no longer a symmetric tensor). For the CDM expressed in the indices $\tilde{\alpha}$ and $\tilde{\beta}$, we may use the Frobenius inner product (4.1) and norm (4.2).

To study the distance dependence of the correlations, we vary the position of clusters A and B, resulting in a position-dependent CDM $\tilde{\rho}^C(x^A_1, x^B_1)$. If the system is translationally invariant, this object depends only on the distance $r = |x^A_1 - x^B_1|$ (the minimal distance for two adjacent clusters is equal to the cluster size n). For a finite system, however, $\tilde{\rho}^C$ will also depend on $(1/2)(x^A_1 + x^B_1)$, at best weakly if the system is long. Strategies for minimizing the dependence on $(1/2)(x^A_1 + x^B_1)$ by taking suitable averages will be discussed in section 4.4.

4.2. DMRG calculation of the CDM

The fact that the Hamiltonian in (3.1) is a one-dimensional pseudo-spin chain allows us to calculate ground state properties with the DMRG [3, 4]. Using the variational MPS formulation of that method (see the appendix for a detailed description), we calculated the ground state of the Hamiltonian in (3.1) for several values of $t_\perp$ and t_c. The framework of MPS also allows the CDM to be calculated efficiently (see section A.2.7 for details). Limiting ourselves to the case $t_\perp = 0$ in this paper, we have calculated the CDM derived from the ground state for distances up to 40 rungs, which is significantly larger than in previous approaches.

We used chain lengths of $N = 100$, 150 and 200 and limited the maximal Hilbert space dimension during the DMRG sweeps to less than ~ 200. This dimension is sufficient to retain all contributions larger than 10^{-6}, with respect to the singular value spectrum on each bond (see section A.2.5), which means that the discarded part of the reduced density matrix at each step is less than 10^{-12}. We believe that this choice is sufficient to represent the ground state good enough to extract power-law correlations. We can trust the CDMs calculated from these ground states up to distances of $r \approx 37$, because for larger r all correlations start to decay exponentially (even if they showed power-law decay for $r \lesssim 37$). This is a well-known artefact of DMRG (see [5], in particular section III.A and figure 12, for an example). The reason for the exponential decay is the limited Hilbert space dimension for the effective state spaces. Even if the dimension is large enough to represent the ground state faithfully, it still imposes an upper bound on the entanglement entropy going through the bond between two sites. Thus, correlations between clusters close to this bond are represented faithfully, while for larger distances the correlations between two clusters are not well captured any more. The distance up to which correlations are represented faithfully can be increased, if desired, by allowing for a larger Hilbert space dimension [9], but for present purposes this was not necessary (as illustrated by figure 12 below).

4.3. Symmetry sectors

All the symmetries of the Hamiltonian are reflected in the CDM, making the CDM block-diagonal, where each block can be labeled uniquely by a set of quantum numbers that are conserved by the Hamiltonian. This means, for Abelian symmetries (which are the only ones we are considering in practice), that the CDM in the original form $\rho^C_{\alpha\beta,\alpha'\beta'}$ fulfills $Q_\alpha + Q_\beta = Q_{\alpha'} + Q_{\beta'}$, where Q_α corresponds to the quantum numbers of state $|\alpha\rangle$, etc. The rearrangement of the CDM into $\tilde{\rho}^C_{\tilde{\alpha}\tilde{\beta}}$ then implies $\Delta Q_{\tilde{\alpha}} = -\Delta Q_{\tilde{\beta}}$ with $\Delta Q_{\tilde{\alpha}} \equiv Q_\alpha - Q_{\alpha'}$ and $\Delta Q_{\tilde{\beta}} \equiv Q_\beta - Q_{\beta'}$. Since $\hat{\rho}^{AB}$ is Hermitian, for every block of the CDM involving $\Delta Q_{\tilde{\alpha}}$ ($\Delta Q_{\tilde{\beta}}$) there has to be a block involving $-\Delta Q_{\tilde{\alpha}}$ ($-\Delta Q_{\tilde{\beta}}$), respectively. Therefore, it is convenient to sort the various parts of the CDM in terms of their change in quantum numbers $\Delta Q \equiv |\Delta Q_{\tilde{\alpha}}| = |\Delta Q_{\tilde{\beta}}|$ and to analyse each symmetry sector individually.

To obtain a general classification of the CDM, we sort the various contributions of the CDM according to the conserved quantum number(s) Q. In the case of the Hamiltonian in (3.1), we consider particle conservation ($Q = \hat{N}_{\mathrm{tot}}$) which breaks the CDM into blocks with well-defined particle transfer $\Delta N \equiv |\Delta N_{\tilde{\alpha}}| = |\Delta N_{\tilde{\beta}}|$ between clusters A and B. The following rms net correlations then are a measure of the correlations with transfer of ΔN particles between A and B (with $\Delta N = 0, 1, 2$):

$$w^2_{\Delta N}(r) = \sum_{\tilde{\alpha}\tilde{\beta}\in\mathcal{S}_{\Delta N}} |\tilde{\rho}^C_{\tilde{\alpha}\tilde{\beta}}(r)|^2, \tag{4.5}$$

where $\sum_{\Delta N=0}^{2} w^2_{\Delta N}(r) = \|\rho^C(r)\|^2$. Here the notation $\tilde{\alpha} \equiv (\alpha\alpha') \in \mathcal{S}_{\Delta N}$ indicates that only pairs of states $(\alpha\alpha')$ are considered that differ by ΔN in particle number (similarly for $\tilde{\beta} \equiv (\beta\beta') \in \mathcal{S}_{\Delta N}$). In the following, we will call correlations involving $\Delta N = 0, 1, 2$ particles *charge-density* correlations (CD), *one-particle* correlations (1P) and *two-particle* correlations (2P), respectively. The following analysis is done for each symmetry sector individually. Depending on the decay of the rms net correlations (4.5), some symmetry sectors may become irrelevant with increasing distance.

4.4. 'Restoration' of numerically broken symmetries

Although we have tried to minimize the effect of boundaries, our numerical methods for calculating the ground state and CDM do not produce strictly translationally invariant results. (In contrast, analyses based on exact diagonalization start from a ground state wave function in which the symmetry (in a finite system) is restored even if there is a symmetry breaking in the thermodynamic limit.) Therefore, we construct the CDM $\tilde{\rho}^C(r)$ for a given distance r from an average over several CDMs $\tilde{\rho}^C(x, x')$ with constant $r = |x - x'|$, where x and x' give the position of the first site of clusters A and B, respectively.

Moreover, if the exact ground state is degenerate under a discrete symmetry, we expect that DMRG breaks this symmetry unless it is implemented explicitly in the code. As mentioned in section 3.2 for the specific models of this paper, we expect a discrete symmetry under interchange of legs for some parameter regimes. Since we did not implement this symmetry explicitly in our code, we also average the CDM by interchanging the legs of the ladder. Thus, all the data analysis presented in subsequent sections will be based on using the following

'symmetry-restored' form of the CDM:

$$\tilde{\rho}^C(r) = \frac{1}{\mathcal{N}} \sum_{xx',|x-x'|=r} \left(\tilde{\rho}^C(x,x') + \tilde{\rho}'^C(x,x')\right), \tag{4.6}$$

where $\tilde{\rho}'^C$ is obtained from $\tilde{\rho}^C$ by interchanging the legs of the ladder, and $\mathcal{N}$ is some normalization factor.

One might argue that it is not sufficient to average over the broken symmetry w.r.t. leg-interchange on the level of the density matrix, but that instead the symmetry should be restored on the level of the ground state wave function. Specifically, for a ground state $|\psi_1\rangle$ (however it is calculated) that breaks this symmetry, we could restore the symmetry in the following way:

$$|\psi^+\rangle = \frac{1}{\sqrt{2}}(|\psi_1\rangle + |\psi_2\rangle), \tag{4.7}$$

where $|\psi_2\rangle = \hat{S}\,|\psi_1\rangle$ and $\hat{S}$ describes the action of interchanging the legs. This would lead to a total density matrix

$$|\psi^+\rangle\langle\psi^+| = \tfrac{1}{2}\left(|\psi_1\rangle\langle\psi_1| + |\psi_2\rangle\langle\psi_2| + |\psi_1\rangle\langle\psi_2| + |\psi_2\rangle\langle\psi_1|\right). \tag{4.8}$$

Now, for two clusters A and B, the first two terms on the rhs yield the CDM of (4.6), whereas the last two terms turn out to be negligible when traced out over all sites except for the two *local* clusters A and B. This follows from $|\psi_1\rangle$ and $|\psi_2\rangle$ being orthogonal, hence $\mathrm{tr}(|\psi_1\rangle\langle\psi_2|) = \langle\psi_2|\psi_1\rangle = 0$, implying that for a long chain with local clusters A and B, the reduced density matrix $\hat{\rho}^{AB,12} \equiv \mathrm{tr}_{x\notin A,B}(|\psi_1\rangle\langle\psi_2|)$ will be very close to zero, since the wave functions of $|\psi_1\rangle$ and $|\psi_2\rangle$ are essentially orthogonal on the sites outside clusters A and B. Consequently, it is sufficient to retain only the first two terms of (4.8), i.e. to restore the broken symmetry on the level of the density matrices only, as done in (4.6).

The preceding arguments could, in principle, be verified explicitly by implementing the rung symmetry in the numerical DMRG code (i.e. excluding the possibility of symmetry breaking by construction).

5. Finding a distance-independent DOB

The goal of this section is to extract a (likely) small set of operators from the CDM, which constitute the system's DOB and whose correlators describe the system's dominant correlations. We will assume in this section that the CDM does not include any broken symmetries as indicated in section 4.4.

5.1. Need for operator bases for clusters A and B

As already mentioned, the CDM (obtained from (4.6)) may be investigated by applying a SVD for each distance individually [1]:

$$\tilde{\rho}^C_{\tilde{\alpha}\tilde{\beta}} = \sum_s w^s\, O^{A,s}_{\tilde{\alpha}} \otimes O^{B,s}_{\tilde{\beta}}, \tag{5.1}$$

or in operator notation:

$$\hat{\rho}^C = \sum_s w^s\, \hat{O}^{A,s} \otimes \hat{O}^{B,s}, \tag{5.2}$$

where $\hat{O}^{A,s}$ and $\hat{O}^{B,s}$ act on clusters A and B, respectively. Here the singular values w^s are strictly positive real numbers. By construction, $\hat{O}^{A,s}$ and $\hat{O}^{B,s}$ form orthonormal sets in their corresponding Hilbert spaces, i.e. $O^{A,s}_{\tilde{\alpha}} = O^{A,s}_{\alpha\alpha'}$ and $O^{B,s}_{\tilde{\beta}} = O^{B,s}_{\beta\beta'}$ form a complete set in the operator space of clusters A and B, respectively, using the inner product as in (4.1). The set includes operators with $w_s = 0$, such as the identity operator, since these will be produced by the SVD. The SVD (5.2) yields for each specific distance r a set of operators $\hat{O}^{A,s}(r)$ and $\hat{O}^{B,s}(r)$ acting on clusters A and B, respectively.

However, the dominant operators so obtained, i.e. the ones with large weight from the SVD of $\tilde{\rho}^C(r)$, are likely not the same as each other for different distances and hence not convenient for characterizing the 'dominant correlations' of the system. What is needed, evidently, is a strategy for reducing the numerous sets of operators $\hat{O}^{A,s}(r)$ and $\hat{O}^{B,s}(r)$ to two 'basis sets of operators' for clusters A and B, respectively, the DOB $\hat{O}^{A,\mu}$ and $\hat{O}^{B,\mu}$, which are r-independent and whose correlators yield the dominant correlations in the system in the spirit of (2.2). (For a translationally invariant system the two sets have to be equal for both clusters A and B, but we will treat them independently in the analysis.) Following the ansatz (2.2) from the Luttinger liquid theory, these operators ought to be distance independent, carrying common correlation content for all distances. Thus, we seek an expansion of $\tilde{\rho}^C(r)$ of the form (2.4), in which *only* the coefficients, not the operators, are r-dependent.

5.2. *Construction of the DOB*

We have explored a number of different strategies for extracting operators from the CDM which carry common information for all distances. We will discuss in detail only one of these, which is rather simple to formulate and reliably yields operator sets with the desired properties. (Several other strategies yielded equivalent results, but in a somewhat more cumbersome fashion.)

The simplest possible strategy one may try is to average over all the CDMs at different distances and to singular-value decompose the resulting crude 'average CDM'. However, since the elements for the CDM are expected to be oscillating functions of r, such a crude average can cancel out important contributions of the CDM. Thus we need a procedure that avoids such possible cancellations. To this end, we construct the following operators, bi-linear in the CDM:

$$\hat{K}^A(r) \equiv \mathrm{tr}_B(\hat{\rho}^{C\dagger}(r)\hat{\rho}^C(r))/\|\hat{\rho}^C\|^2, \tag{5.3a}$$

$$\hat{K}^B(r) \equiv \mathrm{tr}_A(\hat{\rho}^C(r)\hat{\rho}^{C\dagger}(r))/\|\hat{\rho}^C\|^2, \tag{5.3b}$$

with matrix elements

$$K^A_{\tilde{\alpha}\tilde{\alpha}'}(r) = \sum_{\tilde{\beta}} \tilde{\rho}^C_{\tilde{\alpha}\tilde{\beta}}(r)\tilde{\rho}^C_{\tilde{\alpha}'\tilde{\beta}}{}^*(r)/\|\tilde{\rho}^C(r)\|^2, \tag{5.4a}$$

$$K^B_{\tilde{\beta}\tilde{\beta}'}(r) = \sum_{\tilde{\alpha}} \tilde{\rho}^C_{\tilde{\alpha}\tilde{\beta}}(r)\tilde{\rho}^C_{\tilde{\alpha}\tilde{\beta}'}{}^*(r)/\|\tilde{\rho}^C(r)\|^2. \tag{5.4b}$$

We normalize by $\|\tilde{\rho}^C(r)\|^2$ in order to treat the operator correlations of $\tilde{\rho}^C(r)$ for different distances on an equal footing. Note that the eigenvalue decomposition on the Hermitian matrices $K^A(r)$ and $K^B(r)$ (in short K-matrices) yields the same operators $\hat{O}^A(r)$ and $\hat{O}^B(r)$ as the SVD of $\tilde{\rho}^C(r)$, with eigenvalues being equal to singular values squared, up to the additional

normalization factor $\|\tilde{\rho}^C(r)\|^2$. (The reason is that for a matrix of the form $M = usv^\dagger$ we have $MM^\dagger = us^2u^\dagger$ and $M^\dagger M = vs^2v^\dagger$.)

The object $\hat{K}^X$ (for $X = A, B$) is positive-definite, and according to ansatz (2.2), it is expected to have the form

$$\hat{K}^X(r) = \mathcal{N}_K^{-1} \sum_s \frac{|c_s|^2}{r^{2\gamma_s}} \hat{O}^X \hat{O}^{X\dagger}. \tag{5.5}$$

In particular, it no longer contains any oscillating parts (in contrast to (2.2)) and, hence, is suitable for being averaged over r.

Summing up the K^X-matrices over a range R of distances ($r \in R$, where R will be specified below) gives a mean $\bar{K}^X$-matrix for cluster X ($=A, B$), namely $\bar{K}^{X,R} \equiv \sum_{r\in R} \hat{K}^X(r)$. We do not divide the latter expression by the number of terms in the sum (as would be required for a proper mean), as at this stage we are only interested in the operator eigendecomposition,

$$\bar{K}^{X,R} = \sum_\mu w^{R,\mu} (\hat{O}^{X,R,\mu} \otimes \hat{O}^{X,R,\mu\dagger}), \tag{5.6}$$

with the operators normalized such that $\|\hat{O}^{X,R,\mu}\| = 1$. The operator set $\hat{O}^{X,R,\mu}$ gives an orthonormal, r-independent basis for cluster X. In practice, however, many of the $w^{R,\mu}$ (which turn out to be the same for $X = A$ or B) will be very small. Thus, it will be sufficient to work with a truncated set of these operators having significant weight.

To explore the extent to which $\bar{K}^X$ depends on the summation range, we shall study several such ranges: R_{all} includes all distances, R_{short} short distances (first third of distances analysed), R_{int} intermediate distances (second third) and R_{long} long distances (last third). The resulting (truncated) sets of operators can be compared via their mutual overlap matrix $O^{RR'}_{\mu\mu'} = \text{tr}(\hat{O}^{R,X,\mu} \hat{O}^{R',X,\mu'})$, or more simply, by the single number $O^{RR'} = \sum_{\mu\mu'} (O^{RR'}_{\mu\mu'})^2$, which may be interpreted as the dimension of the common subspace of the two operator sets. The value of $O^{RR'}$ ranges from 0 to $\dim(\hat{O}^{R,X,\mu})$. By comparing $O^{RR'}$ for the different distance ranges, additional clues can be obtained about how the relative weight of correlations evolves from short to long distances. (Such a comparison is carried out in table 1 below.)

5.3. *Definition of f-matrix*

Once two convenient DOBs for each cluster, the sets of operators $\hat{O}^{A,\mu}$ and $\hat{O}^{B,\mu}$, have been found, the CDM can be expanded in terms of these bases as in (2.4),

$$\tilde{\rho}^C_{\tilde{\alpha}\tilde{\beta}}(r) = \sum_{\mu\mu'} f^{\mu,\mu'}(r) O^{A,\mu}_{\tilde{\alpha}} O^{B,\mu'}_{\tilde{\beta}}, \tag{5.7}$$

with matrix elements

$$f^{\mu,\mu'}(r) \equiv \sum_{\tilde{\alpha}\tilde{\beta}} \tilde{\rho}^C_{\tilde{\alpha}\tilde{\beta}}(r) O^{A,\mu}_{\tilde{\alpha}} O^{B,\mu'}_{\tilde{\beta}}. \tag{5.8}$$

For complete operator bases $\hat{O}^{A,\mu}$ and $\hat{O}^{B,\mu'}$, by definition, the set of amplitudes squared sum up to the norm of the CDM:

$$\sum_{\mu\mu'} |f^{\mu,\mu'}(r)|^2 = \|\tilde{\rho}^C(r)\|^2. \tag{5.9}$$

Table 1. Comparison of the operator sets on cluster A for a filling of $\nu = 0.286$, calculated for chain length $N = 100$. (The results for $\nu = 0.248$ and other chain lengths are similar, with only minor differences.) The first and second columns of the table give the number of operators kept and the corresponding smallest singular value of the set of operators $\hat{O}^{A,R_{\rm all},\mu}$ obtained from the full range of distances $R_{\rm all}$. The other three columns show $O^{R_{\rm all}R_{\rm short}}$, $O^{R_{\rm all}R_{\rm int}}$ and $O^{R_{\rm all}R_{\rm long}}$ for the given number of operators.

Number of operators	$w^{R_{\rm all},\mu}/w^{R_{\rm all},1}$	$O^{R_{\rm all}R_{\rm short}}$ (short)	$O^{R_{\rm all}R_{\rm int}}$ (intermediate)	$O^{R_{\rm all}R_{\rm long}}$ (long)
1	1	1	0.99	1
2	0.784 122	1.99	2	2
3	0.579 242	2.99	3	3
4	0.176 043	3.99	4	4
5	0.011 250	5	5	4.99
6	0.003 040	6	6	5.99
7	0.000 004	7	6	6
8	0.000 001	8	6	6
9	0.000 001	9	6	6
10	0.000 001	10	6	6

However, as alluded to above, we expect that the dominant correlators can be expressed in terms of a *truncated* set of dominant operators. If the sum on the lhs of (5.9) is restricted to this truncated set, its deviation from the rhs gives an estimate of how well $\tilde{\rho}^C$ is represented by the DOB. It will turn out that only a handful of dominant operators (typically 4 or 6) are needed, implying very significant simplifications in the analysis. Thus, the data analysis will be done in terms of the matrices $f^{\mu,\mu'}(r)$ (in short 'f-matrix') based on the DOB.

5.4. Fourier analysis and decay of f-matrix

According to the expectations expressed in (2.2), the elements of the f-matrix are expected to be products of oscillating and decaying functions of r. The corresponding dominant wave vectors can be identified via Fourier transform on each element of the f-matrix. For an oscillating function times a monotonically decaying envelope, the peaks of the Fourier spectrum of the oscillating function will be broadened by the presence of the envelope. To minimize this unwanted broadening, we introduce a rescaled f-matrix (denoted by a tilde), $\tilde{f}^{\mu,\mu'}(r) = u(r) f^{\mu,\mu'}(r)$, where the positive weighting-function $u(r)$ is chosen such that all values of $|\tilde{f}^{\mu,\mu'}(r)|$ are of the same order, and we Fourier decompose the rescaled $\tilde{f}$-matrix as $\tilde{f}^{\mu,\mu'}(k) = \sum_r \mathrm{e}^{-\mathrm{i}kr} \tilde{f}^{\mu,\mu'}(r)$. Its norm $\|\tilde{f}(k)\|^2 = \sum_{\mu\mu'} |\tilde{f}^{\mu,\mu'}(r)|^2$, plotted as a function of k, will contain distinct peaks that indicate which wave vectors characterize the dominant correlations. Subsequently, the elements of the f-matrix can be fitted to the form

$$f^{\mu,\mu'}(r) = \sum_j A^{[j]}_{\mu,\mu'} \mathrm{e}^{\mathrm{i}k_j r} f_j(r), \tag{5.10}$$

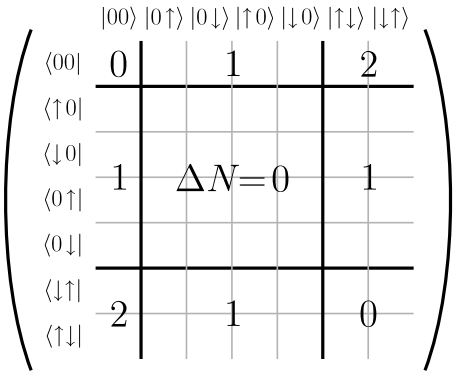

Figure 2. The symmetry sectors of an operator acting on a cluster of two rungs in the basis $|00\rangle$, $|0\uparrow\rangle$, $|0\downarrow\rangle$, $|\uparrow 0\rangle$, $|\downarrow 0\rangle$, $|\uparrow\downarrow\rangle$, $|\downarrow\uparrow\rangle$ in pseudo-spin notation.

where $A^{[j]}_{\mu,\mu'}$ are complex amplitudes, $f_j(r)$ describes the decay with distance (e.g. $f_j(r) = r^{-\gamma_j}$ or e^{-r/r_j} for power-law or exponential decay, respectively) and k_j is a set of dominant wave vectors. The latter appear pairwise in combinations $(+k; -k)$, since $f^{\mu,\mu'} \in \mathbb{R}$, which implies $A^{[i]}_{\mu,\mu'} = A^{[j]*}_{\mu,\mu'}$ for $k_i = -k_j$. The results of such a fit for each pair of dominant operators $\hat{O}^{A,\mu}$ and $\hat{O}^{B,\mu'}$ are the final outcome of our analysis, since it contains the information needed to check the applicability of ansatz (2.1).

6. Numerical results: general remarks

In this section, we illustrate the analysis proposed above for the model introduced in section 3. We will focus on the limiting case of large t_c (called 'paired limit' in [2], see section IV.B therein), which we expect to have the most complex behaviour among all three limiting cases introduced in [1, 2]. After some preliminary analysis, we will discuss in section 7 each of the three symmetry sectors (CD, 1P and 2P) characterized by the operators' fermion number and, in section 8, compare our present results with those found in [2] using a different method.

6.1. Specification of clusters A and B

For the following analysis, it is convenient to take the size of clusters A and B to be two rungs, because clusters of at least that size allow for up to two particles in one cluster (due to infinite nearest-neighbour repulsion). Thus, correlations involving $\Delta N = 0, 1, 2$ are possible, i.e CD, 1P and 2P correlations, respectively. Note that larger clusters can be studied, but that would significantly increase numerical costs. Taking into account the infinite nearest-neighbour repulsion, clusters of size two have a seven-dimensional Hilbert space spanned by the kets $|00\rangle$, $|0\uparrow\rangle$, $|0\downarrow\rangle$, $|\uparrow 0\rangle$, $|\downarrow 0\rangle$, $|\uparrow\downarrow\rangle$, $|\downarrow\uparrow\rangle$, where the first (second) entry corresponds to the first (second) rung, 0 represents an empty rung and $\uparrow$ and $\downarrow$ a fermion on the upper and lower legs in pseudo-spin notation (recall that we are dealing with spinless fermions). The space of operators acting on a cluster has dimension $7^2 = 49$, where the subspaces for $\Delta N = 0$, 1 or 2 have dimensions 21, 24 and 4, respectively, as depicted schematically in figure 2.

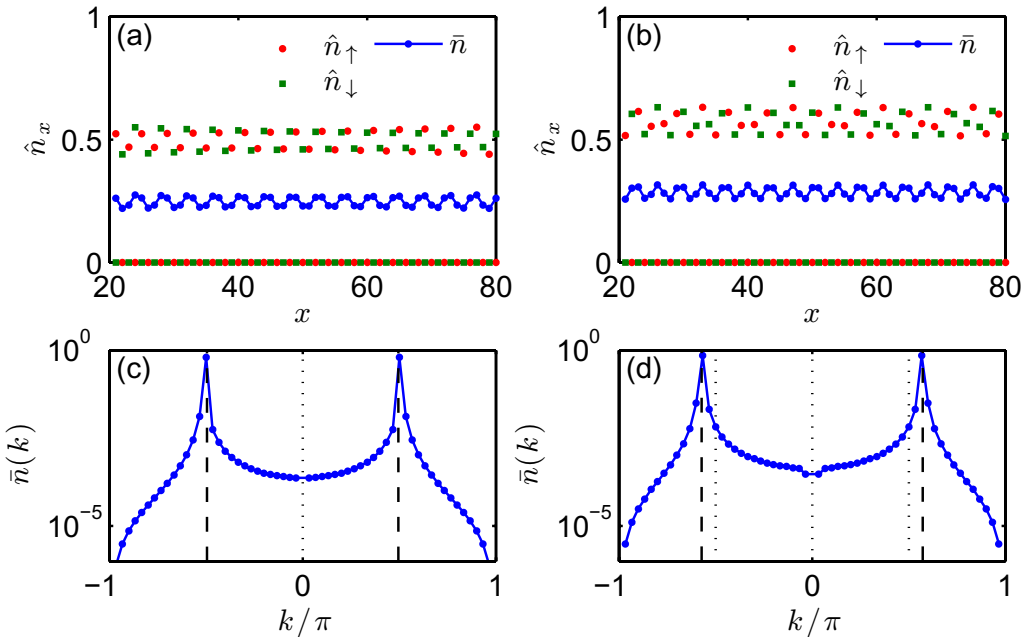

Figure 3. The average occupation along the legs of the ladder for a filling of $\nu = 0.248$ ((a) and (c)) and a filling of $\nu = 0.286$ ((b) and (d)). In ((a) and (b)), we show the average occupation $\hat{n}_\uparrow$ on the upper leg (red) and $\hat{n}_\downarrow$ on the lower leg (green), with every second value being zero. The end regions $i = 1, \ldots, 20$ and $i = 81, \ldots, 100$ were excluded in the figures and also in the analysis, as these are affected by the smooth open boundary condition. The leg symmetrized occupation $\bar{n} = \frac{1}{2}(\hat{n}_\uparrow + \hat{n}_\downarrow)$ (blue, the same for the upper and lower legs) eliminates this strong even–odd alternation but still shows small modulations. This can be seen in detail in the Fourier transform of the symmetrized occupation in (c) and (d). There is a clear peak at $k = \pm 2k_F$ (dashed vertical lines).

6.2. Average site occupation

As a first check of the influence of the boundaries, we investigate the average site occupation on the ladder. It is expected to be uniform in a translationally invariant system. However, there are two ways in which our calculation breaks translational symmetry, which cause residual oscillations in the density of particles along the ladders.

Firstly, there is the spontaneous breaking of the pair flavour symmetry described in section 3.2. In the ground state produced by DMRG, all pairs have the same flavour, so only one of the two sublattices actually has any fermions on it. Thus a strong alternation in the density is observed between one leg for even rungs and the other leg for odd rungs; this can be taken care of by the symmetrization with respect to legs (as in (4.6)).

Secondly, translational symmetry is broken due to finite size in the DMRG calculation. This induces oscillations in the average occupation as a function of x (see figure 3), whose period is clearly dependent on the filling. In fact, their period is $2k_F$, so they may be interpreted as Friedel-like oscillations caused by the boundaries. Although the amplitude of density oscillation appears rather flat in the central portion of the system, it does have a minimum there; so we expect that the amplitude in the centre of the system would vanish in a sufficiently large system.

Although the intent of the smooth boundary conditions is to minimize effects such as these oscillations, in fact, their amplitude appeared to be of about the same strength independent of whether we used smooth or plain open boundary conditions. We suspect, however, that the amplitude could be reduced by further careful optimization (not attempted here) of the parameters of the smooth boundary conditions.

6.3. Rms net correlations $w_{\Delta N}(r)$

The next basic step is to identify the leading correlations in terms of the rms net correlations $w_{\Delta N}$ defined in (4.5). These reveal which sectors of correlations dominate at large distances. The results (see figure 4) show that the rms net correlations decay exponentially in the 1P sector, whereas they decay algebraically in both the CD and 2P sectors, consistent with Cheong and Henley's work [2]. The latter two correlations are comparable in size over a significant range of distances, but for the fillings that we investigated, 2P correlations ultimately dominate over CD correlations at the largest distances.

Both the CD and 2P rms net correlations can be fitted to power laws, with the exponent dependent on the filling. The fitting of oscillating data—even if weakly oscillating—to a monotonic power law has to be done very carefully. As the correlations have the largest absolute value at short distances, the fitting is sensitive to these values and thus to the precise range of the fitting interval $[r_1, r_2]$ (compare the oscillations of the rms net correlations within the first ten sites in figure 4). Thus, we perform fits for $\mathcal{N}_{r_1}$ different values of r_1 between 2 and $2+\pi/k_{\mathrm{F}}$ (i.e. covering one period of the oscillation), with r_2 fixed to the maximal distance available. Denoting the fitting result for a given r_1 by $\gamma[r_1]$, we take the mean value of the latter as our fitting result and the variance as the error of our fitting:

$$\gamma = \frac{1}{\mathcal{N}_{r_1}} \sum_{r_1=2}^{2+\pi/k_{\mathrm{F}}} \gamma[r_1], \qquad \delta\gamma = \left[\frac{1}{\mathcal{N}_{r_1}} \sum_{r_1=2}^{2+\pi/k_{\mathrm{F}}} (\gamma - \gamma[r_1])^2 \right]^{1/2}. \tag{6.1}$$

The rms net correlations in each sector are monotonic and only weakly modulated, even though the dominant correlation functions and the dominant parts of the CDM itself are oscillating (as will be discussed in more detail in section 7.1; see e.g. figure 7). This implies that the correlations in each sector can be represented by a linear combination of correlation functions (associated with different operators) that oscillate out of phase, in such a way that in the sum of their squared moduli the oscillations more or less average out, resulting in an essentially monotonic decay with r, as expected according to (2.3).

We will next apply the analysis proposed in section 5.2 to the respective symmetry sectors (which will provide more exact fits of the exponents of the power law decays). The analysis in any sector consists of two stages. Firstly, following section 5.2, we try to find an optimal truncated basis that describes best the dominant correlations. Secondly, we examine the f-matrix of section 5.3 (i.e. represent the CDM in the truncated basis) to see the nature of its r dependence and to fit this to an appropriate form, following section 5.4.

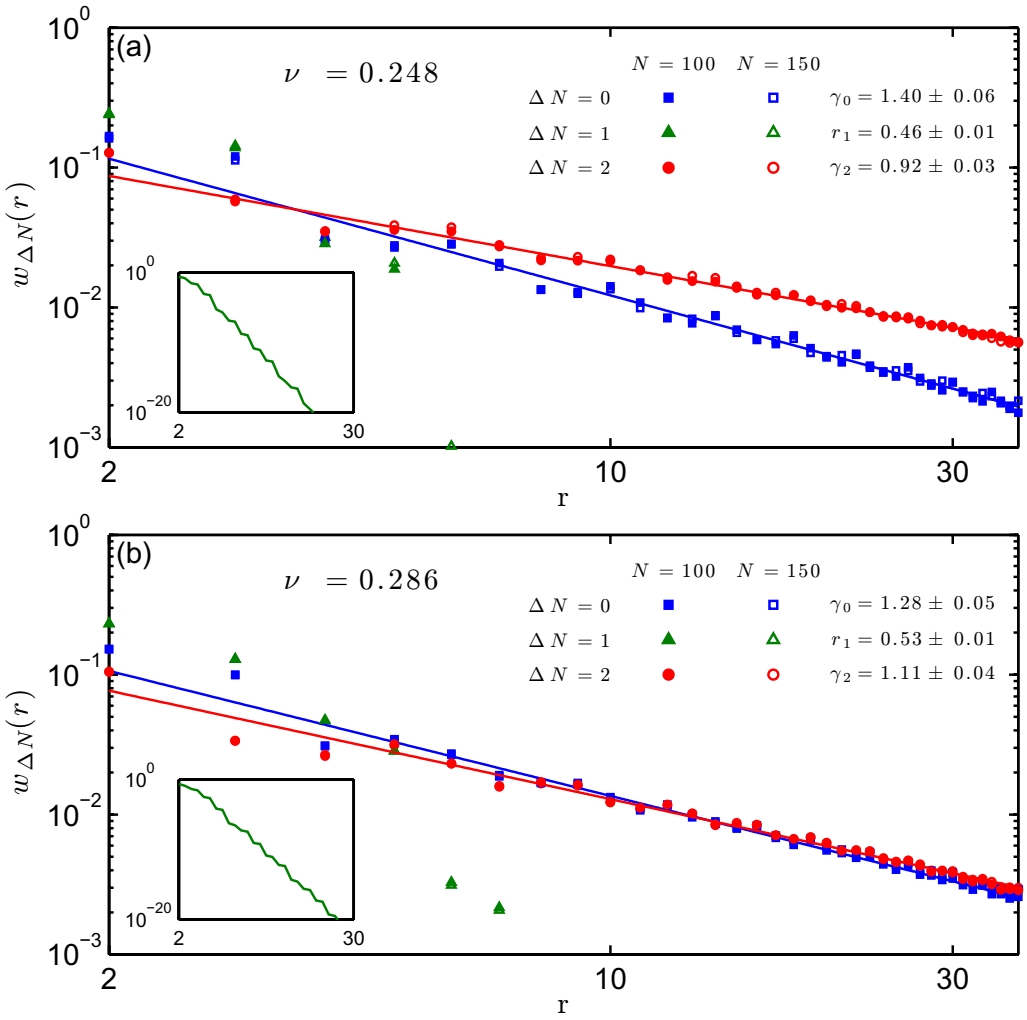

Figure 4. The rms net correlations of (4.5), plotted as a function of distance for a filling of (a) $\nu = 0.248$ and (b) $\nu = 0.286$, for chain lengths $N = 100$ (filled symbols) and $N = 150$ (open symbols). The symmetry sectors are $\Delta N = 0$ (squares, no particle transfer, CD), $\Delta N = 1$ (triangles, transfer of one particle, 1P) and $\Delta N = 2$ (dots, transfer of two particles, 2P). We see that CD and 2P correlations decay as power laws ($r^{-\gamma}$, solid lines) with small residual oscillations at $k = 2k_F$, while the 1P correlations show exponential decay (e^{-r/r_1}, see the semi-logarithmic plot in the inset). The results for different chain lengths differ only slightly (for most data points no open symbols are visible, because they overlap fully with filled symbols). Consequently, the values obtained for γ_0, r_1 and γ_2 are the same for both chain lengths.

7. Numerical results: symmetry sectors

7.1. Charge-density correlations

7.1.1. Operator basis. The following analysis to obtain the DOB for the charge-density correlations is independent of filling and chain length. We obtain exactly the same DOB for

different fillings and chain lengths, but of course the coefficients of the f-matrix depend on the filling (not on the chain length). The functional form of the f-matrix is investigated in the next section.

First, we calculated the mean K-matrices $\bar{K}^{A,R}$ and $\bar{K}^{B,R}$ from $\bar{\rho}_R^C$ defined in (5.3*a*) and (5.3*b*) and obtained operator sets from their eigenvalue decomposition, using various distance ranges. In order to construct the DOB, we used the diagnostic described in section 5.2. In presenting the results, we limit ourselves to cluster A as the results for cluster B are completely analogous. The operator set $\hat{O}^{A,R_{\text{all}},\mu}$ corresponding to the full range of distances R_{all} (specified in section 5.2) is used as a reference set to be compared with the operator sets obtained from R_{short}, R_{int} and R_{long}. The results are given in table 1. We see that, for intermediate or long distances, the effective dimension ($O^{R_{\text{all}}R_{\text{int}}}$ and $O^{R_{\text{all}}R_{\text{long}}}$) of the common operator space shared between the operator set $\hat{O}^{A,R_{\text{all}},\mu}$ and the operator sets $\hat{O}^{A,R_{\text{int}},\mu}$ and $\hat{O}^{A,R_{\text{long}},\mu}$, respectively, saturates at six even if a larger operator space is allowed. Similarly, also the short-distance operator set $\hat{O}^{A,R_{\text{short}},\mu}$ agrees best with the other three operator sets at dimension six: a further increase of the number of operators, however, adds only operators in the short-range sector of the CDM. Hence, we construct the DOB as a six-dimensional operator set. Within this reduced operator space, all dominant correlations are well captured, as can be seen from the relative weights of table 1. For the resulting truncated basis set, equation (5.9) holds up to a relative deviation of the order of $\mathcal{O}(10^{-5})$.

Investigating the DOB in more detail reveals that it can be split into two sectors, classified by their symmetry with respect to interchanging the legs of the ladder, i.e. the operators obey $\hat{S}\hat{O}^{A,R_{\text{all}},\mu} = \pm\hat{O}^{A,R_{\text{all}},\mu}$, with $\hat{S}$ describing the action of interchanging legs. The two subsets contain three operators each, which have positive or negative parity with respect to $\hat{S}$, respectively. It turns out that all six operators are linear combinations of operators having matrix elements on the diagonal only, in the representation of figure 2. Moreover, together with the unit matrix they span the full space of diagonal operators (therefore the dimension of $6 = 7 - 1$). Explicitly, the symmetric operators are given by

$$\hat{O}^1 = \tfrac{1}{\sqrt{12}}\left(-\hat{n}_{0,x}\hat{n}_{\uparrow,x+1} - \hat{n}_{\uparrow,x}\hat{n}_{0,x+1} + 2\hat{n}_{\uparrow,x}\hat{n}_{\downarrow,x+1} + \text{leg symmetrized}\right), \tag{7.1a}$$

$$\hat{O}^2 = \tfrac{1}{2}\left(\hat{n}_{0,x}\hat{n}_{\uparrow,x+1} - \hat{n}_{\uparrow,x}\hat{n}_{0,x+1} + \text{leg symmetrized}\right), \tag{7.1b}$$

$$\hat{O}^3 = \tfrac{1}{\sqrt{42}}\left[-6\hat{n}_{0,x}\hat{n}_{0,x+1} + \left(\hat{n}_{0,x}\hat{n}_{\uparrow,x+1} + \hat{n}_{\uparrow,x}\hat{n}_{0,x+1} + \hat{n}_{\uparrow,x}\hat{n}_{\downarrow,x+1} + \text{leg symmetrized}\right)\right] \tag{7.1c}$$

and the antisymmetric operators by

$$\hat{O}^4 = \tfrac{1}{\sqrt{2}}\hat{n}_{0,x}\left(\hat{n}_{\uparrow,x+1} - \hat{n}_{\downarrow,x+1}\right), \tag{7.2a}$$

$$\hat{O}^5 = \tfrac{1}{\sqrt{2}}\left(\hat{n}_{\uparrow,x} - \hat{n}_{\downarrow,x}\right)\hat{n}_{0,x+1}, \tag{7.2b}$$

$$\hat{O}^6 = \tfrac{1}{\sqrt{2}}\left(\hat{n}_{\uparrow,x}\hat{n}_{\downarrow,x+1} - \hat{n}_{\downarrow,x}\hat{n}_{\uparrow,x+1}\right), \tag{7.2c}$$

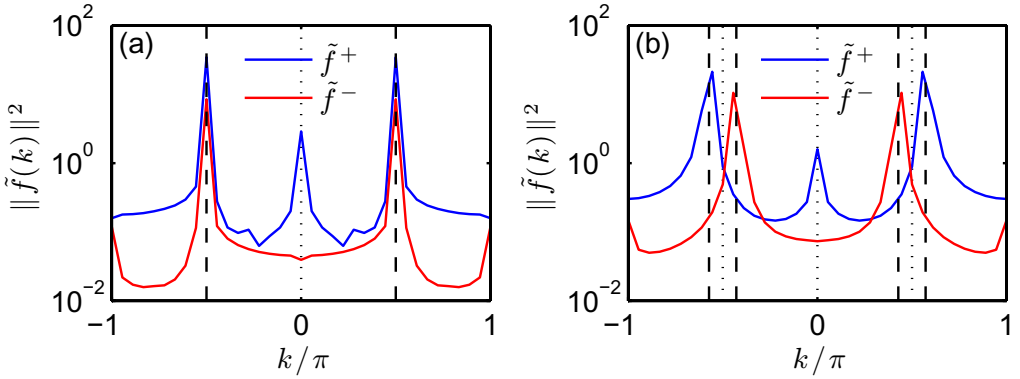

Figure 5. Fourier transform of the rescaled f-matrix $\tilde{f}$ for CD correlations based on operators chosen from a reduced six-dimensional operator space, for a filling of (a) $\nu = 0.248$ and (b) $\nu = 0.286$. We obtain these Fourier spectra from the rescaled f-matrix $\tilde{f}^{\mu,\mu'}(r) = r^{\gamma''} f^{\mu,\mu'}(r)$, with γ'' extracted from a power law fit on $|f^{\mu,\mu'}(r)|$. The Fourier spectrum breaks up into a contribution coming from the operators symmetric or antisymmetric under leg interchange, labelled $\tilde{f}^+$ (blue) and $\tilde{f}^-$ (red), respectively. The spectrum of $\tilde{f}^+$ shows strong peaks at $k = \pm 2k_F$ (dashed lines) and a smaller peak at $k = 0$ with $k_F/\pi = \nu$. The spectrum of $\tilde{f}^-$, having peaks at $k = \pm 2k_F + \pi$ (dashed lines) and $k = \pi$, is shifted w.r.t. $\tilde{f}^+$ by π. For a filling close to $\frac{1}{4}$ the dominant peaks of $\tilde{f}^\pm$, at $k = \pm 2k_F$ and $k = \pm 2k_F + \pi$, are nearly at the same position.

where $\hat{n}_0 = (1 - \hat{n}_\uparrow - \hat{n}_\downarrow)$. We use this operator basis for both cluster A and cluster B. If we calculate the f-matrix (5.7) based on these operators, we see that it breaks into two blocks corresponding to their symmetry with respect to leg interchange.

7.1.2. f-matrix elements: oscillations and decay. We now turn to extracting the distance dependence of the dominant correlation in this symmetry sector, which is now visualizable since we have drastically reduced the operator space to six dimensions. All the relevant information is contained in the f-matrix and its Fourier transform. The first step is to identify the oscillation wave vector(s) k to be used as initial guesses in the fit. A general method is to plot the Fourier spectrum $\|\tilde{f}(k)\|$ of the rescaled f-matrix (figure 5). When using a logarithmic scale for the vertical axis, even sub-leading contributions show up clearly. We find that the spectra belonging to the symmetric and anti-symmetric operators are shifted against each other by π. This relative phase shift implies a trivial additional distance dependence of $e^{i\pi r}$ of $f^-(r)$ with respect to $f^+(r)$, reflecting the different parity under leg interchange of the two operator sets. We have found it convenient to undo this shift by redefining $f^-(r)$, the part of the f-matrix belonging to the anti-symmetric operators, to $e^{i\pi r} f^-(r)$. The resulting combined Fourier spectrum for f^+ and $e^{i\pi r} f^-$ has strong peaks at $k = 2k_F$ and a smaller peak at $k = 0$, in agreement with the result of [2].

Based on the Fourier spectrum, we rewrite the fitting form (5.10) as

$$f^{\mu,\mu'}(r) = A_{\mu\mu'} r^{-\gamma} \cos(kr + \phi_{\mu\mu'}) + B_{\mu\mu'} r^{-\gamma'}, \tag{7.3}$$

with real numbers $A_{\mu\mu'} > 0$ and $B_{\mu\mu'}$, where we expect $\gamma' > \gamma$, due to the relative sharpness of the peaks in the Fourier spectrum. The nonlinear fitting is done in several steps to also include

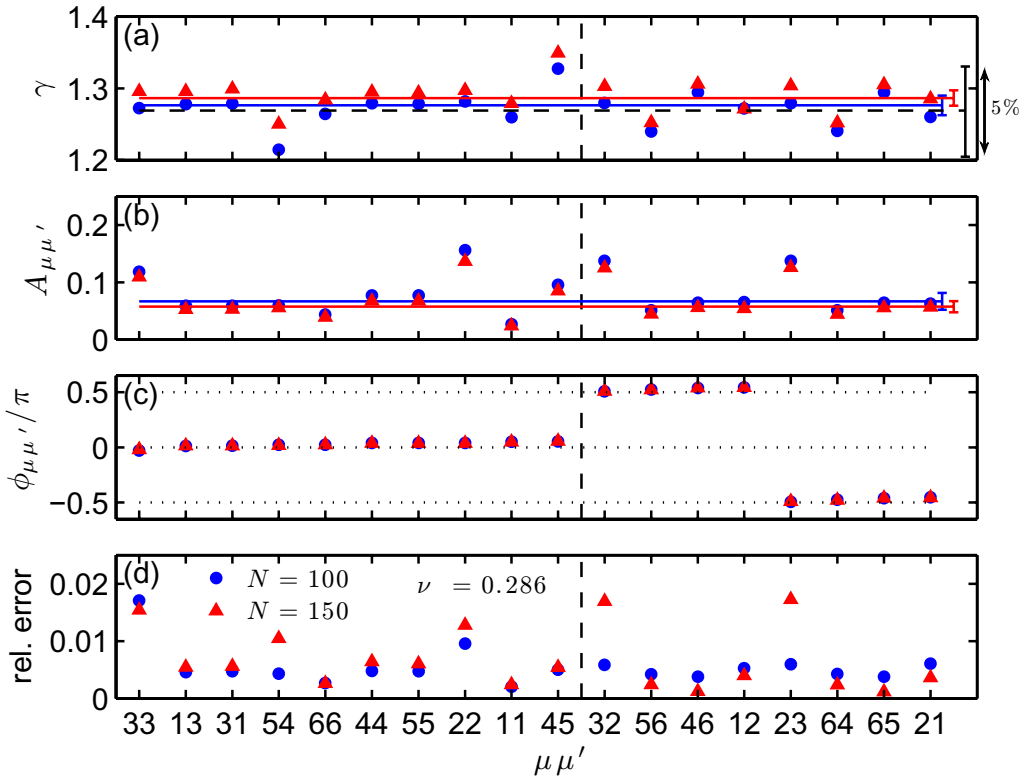

Figure 6. The results of the fit in (7.3) to the 18 independent elements $f^{\mu,\mu'}$ of the f-matrix, labelled along the horizontal axis by the index pair $\mu\mu'$, for $\Delta N = 0$ at filling $\nu = 0.286$ for chains with length $N = 100$ (blue circles) and $N = 150$ (red triangles). The results for $\nu = 0.248$ are qualitatively the same. (a) γ, (b) $A_{\mu\mu'}$, (c) $\phi_{\mu\mu'}$ and (d) the overall fit error ϵ of (7.4). The phase $\phi_{\mu\mu'}$ is defined such that it lies in the interval $[-\pi, \pi]$. The matrix elements have been grouped according to their relative phases $\phi_{\mu\mu'}$ (separated by the vertical dashed line), which clearly indicate cos and sin behaviour for $\phi_{\mu\mu'} = 0$ and $\phi_{\mu\mu'} = \pm\frac{\pi}{2}$, respectively. The exponent $\gamma_0 = 1.277$ and the amplitude $A = 0.066$ obtained from the single fit (7.5) (which was averaged over fitting ranges $[r_1, r_2]$ according to (6.1)), are shown by the solid lines in (a) and (b), respectively; the small error bars on the right of these panels show the corresponding variances $\delta\gamma_0 = \pm 0.013$ and $\delta A = \pm 0.003$. For comparison, (a) also shows the rms exponent $\gamma_0^{\mathrm{rms}} = 1.28$ (dashed line) and its uncertainty ± 0.05 (largest error bar on the right), as determined in figure 4(b).

the decaying part at long distances on an equal footing. Firstly, the data are multiplied by $r^{+\gamma''}$, where we obtained γ'' from a simple power-law fit, in order to be able to fit the oscillations for all distances with comparable accuracy. Then we fit the rescaled data to (7.3), where initially we use the information from the Fourier spectrum in keeping k fixed to $k = 2k_{\mathrm{F}}$, but finally also release the constraint on k. As in section 6.3, we average the results of this procedure for fitting ranges $[r_1, r_2]$, with r_1 ranging from 2 to $2 + \pi/k_{\mathrm{F}}$, see (6.1).

The results of this fitting procedure are depicted in figure 6 for $\nu = 0.286$, for all 18 nonzero elements of the f-matrix. Figure 6(a) shows the leading power-law exponents γ;

they are distributed within a window of about 5% around the corresponding rms value $\gamma_0^{\rm rms} = 1.28 \pm 0.05$ (figure 6(a), dashed line) obtained in figure 4(b). The k-vectors from the nonlinear fit are close to $k = 2k_{\rm F}$ and deviate from this by less than 1%. The fit results for γ' (not shown) always yielded $\gamma' > \gamma$ (with γ' ranging between 2 and 10), but are less reliable than for γ, because the quicker decay implies a comparatively stronger influence from the small-r regime. The relative errors ϵ for the individual matrix elements $f^{\mu,\mu'}$, defined as

$$\epsilon^2 = \sum_r (f^{\mu,\mu'}(r) - f^{\rm fit}(r))^2 / r^{-2\gamma"}, \tag{7.4}$$

are depicted in figure 6(d) and are always smaller than 2%.

Since most of the exponents γ and amplitudes $A_{\mu\mu'}$ are of comparable size, we have also performed a fit of the f-matrix elements to a *single* γ_0 and A (as well as a single γ_0' and B for the second term) for all the f-matrix elements, using the ansatz:

$$f(r) = Ar^{-\gamma_0} \begin{pmatrix} \begin{pmatrix} \cos(kr) & \sin(kr) & \cos(kr) \\ -\sin(kr) & \cos(kr) & -\sin(kr) \\ \cos(kr) & \sin(kr) & \cos(kr) \end{pmatrix} & 0 \\ 0 & {\rm e}^{{\rm i}\pi r} \begin{pmatrix} \cos(kr) & \cos(kr) & \sin(kr) \\ \cos(kr) & \cos(kr) & \sin(kr) \\ -\sin(kr) & -\sin(kr) & \cos(kr) \end{pmatrix} \end{pmatrix} + Br^{-\gamma_0'}. \tag{7.5}$$

The form of the matrices in the two blocks was obtained by inserting into (7.3) the explicit values of the phases $\phi_{\mu\mu'}$ determined from the previous fit and summarized in figure 6. Fitting to (7.5) gives an error of about 10%, with the largest errors arising for the f-matrix elements where $A_{\mu\mu'}$ deviates strongly from A (see figure 6). Averaging over fitting ranges $[r_1, r_2]$ according to (6.1), we find $\gamma_0 = 1.277 \pm 0.013$ and $A = 0.066 \pm 0.003$ (indicated by solid lines and small error bars in figures 6(a) and (b), respectively). The values of γ_0' and B are unreliable in that the results from several fittings differ by about 30%, but still it holds that $\gamma_0' > \gamma_0$, with γ_0' ranging between 1.7 and 2.3. The overall error estimate of (7.4) yields $\epsilon \approx 0.1$, i.e. an error of order 10%, the largest contributions arising from those f-matrix elements for which $A_{\mu\mu'}$ deviates most strongly from the average A.

The form of (7.5) allows us to understand why the rms net correlations displayed in figure 4 show some residual oscillations, instead of decaying completely smoothly, as anticipated in section 2. The reason is that (7.5) contains ten $\cos(kr)$ terms but only eight $\sin(kr)$ terms. Although any two such terms oscillate out of phase, as illustrated in figure 7, the cancellation of oscillations will thus not be complete. Instead, the rms net correlations contain a factor $[8 + 2\cos^2(kr)]^{1/2}$ (compare with (4.5)), which produces relative oscillations of about 10%, in accord with figure 4. (The fact that the total numbers of $\cos(kr)$ and $\sin(kr)$ terms are not equal is to be expected: the total operator Hilbert space per cluster is limited, and its symmetry subspaces might have dimensions not a multiple of 4.)

For each pair of wave vectors $\pm k$ in each parity sector, the effective operator basis per cluster can be reduced even further, from three operators to one conjugate pair of operators. This can be seen by rewriting (7.5) as follows:

$$f(r) = Ar^{-\gamma_0} \left[{\rm e}^{{\rm i}kr} \begin{pmatrix} f_+ & 0 \\ 0 & {\rm e}^{{\rm i}\pi r} f_- \end{pmatrix} + {\rm c.c.} \right] + Br^{-\gamma_0'}, \tag{7.6}$$

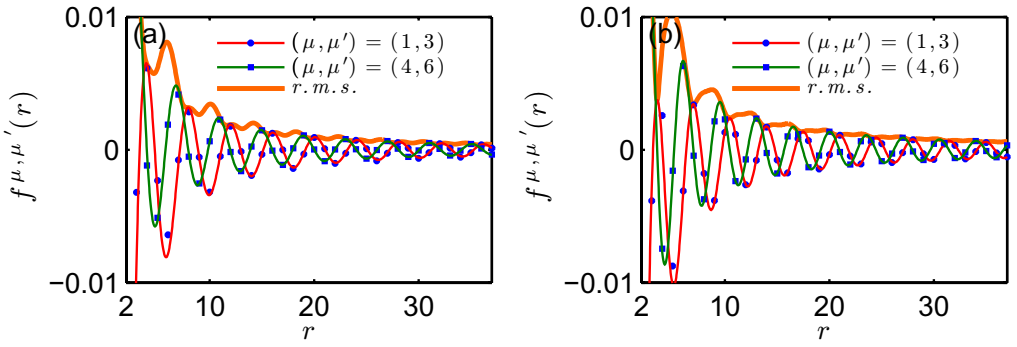

Figure 7. Two entries of the f-matrix for (a) $\nu = 0.248$ and (b) $\nu = 0.286$ fitted to the form in (7.3). The single points (blue circles and squares) are data points from the f-matrix and the lines (red and green) are the result of the fitting. They evidently oscillate with a relative phase of $\Delta\phi = \pi/2$. As a result, their contribution to the rms net correlations, $(|f^{1,3}|^2 + |f^{4,6}|^2)^{1/2}$, shown by the thick orange curve, has only small oscillations at large distances.

with the matrices f_+ and f_- defined as

$$f_+ = \frac{1}{2}\begin{pmatrix} 1 & -\mathrm{i} & 1 \\ \mathrm{i} & 1 & \mathrm{i} \\ 1 & -\mathrm{i} & 1 \end{pmatrix}, \quad f_- = \frac{1}{2}\begin{pmatrix} 1 & 1 & -\mathrm{i} \\ 1 & 1 & -\mathrm{i} \\ \mathrm{i} & \mathrm{i} & 1 \end{pmatrix}. \tag{7.7}$$

Note that both f_+ and f_- are matrices of rank one with eigenvalues $\frac{3}{2}$, 0 and 0. The eigenvectors with eigenvalue $\frac{3}{2}$ are $\frac{1}{\sqrt{3}}(1, \mathrm{i}, 1)$ and $\frac{1}{\sqrt{3}}(1, 1, \mathrm{i})$, respectively. Thus, by transforming to an operator basis in which $f_\pm$ is diagonal, one finds that in both the even and the odd sector, the dominant correlations are actually carried by only a pair of operators, namely $\frac{1}{\sqrt{3}}(\hat{O}^1 + \mathrm{i}\hat{O}^2 + \hat{O}^3)$ and its Hermitian conjugate, and $\frac{1}{\sqrt{3}}(\hat{O}^4 + \hat{O}^5 + \mathrm{i}\hat{O}^6)$ and its Hermitian conjugate, respectively. This result, whose precise form could hardly have been anticipated *a priori*, is a pleasing illustration of the power of a CDM analysis to uncover nontrivial correlations.

7.2. One-particle correlations

The correlations in the 1P sector are exponentially decaying, as already mentioned in section 6.3. The reason for this was given in [1] and is the key to understanding the operators and correlations in this sector. In the limit where the fermions are all paired, the only possible way to annihilate one at x and create one at $x' > x$, such that the initial and final states are both paired, is that every rung in the interval (x, x') has a fermion (necessarily on alternating legs). These fermions can be grouped as pairs in two different ways: $(x, x+1)$, $(x+2, x+3)$, ..., $(x'-2, x'-1)$ in the initial state and $(x+1, x+2)$, ..., $(x'-1, x')$ in the final state. (Note that this requires that x and x' have the same parity.) Cheong and Henley [1] showed that the probability of such a run of filled sites decays exponentially with its length.

Applying the operator analysis in this sector using the eigenvalue decomposition in (5.6) gives a series of fourfold degenerate eigenvalues for both clusters; see table 2 for cluster A. The table for cluster B is exactly the same. For a specific eigenvalue, also the operators for cluster

Table 2. Comparison of the 1P operator sets on cluster A for a filling of $\nu = 0.286$, using the same conventions as for table 1.

Number of operators	$w^{R_{\mathrm{all}},\mu}/w^{R_{\mathrm{all}},1}$	$O^{R_{\mathrm{all}}R_{\mathrm{short}}}$ (short)	$O^{R_{\mathrm{all}}R_{\mathrm{int}}}$ (intermediate)	$O^{R_{\mathrm{all}}R_{\mathrm{long}}}$ (long)
4	1	4	4	4
8	0.297 162	8	8	8
12	0.014 661	12	12	12
16	0.000 402	16	16	16
20	0.000 001	19.97	19.95	19.31

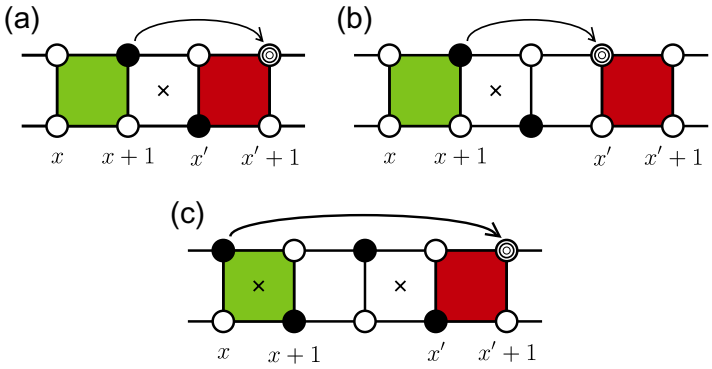

Figure 8. Three configurations of bound pairs contributing to 1P correlations for a distance (a) $r = 2$ and ((b) and (c)) $r = 3$. Clusters A and B are depicted by the green and red squares, respectively. Fermions are depicted by black circles, empty lattice positions by white circles and the position where a fermion will be created is depicted by concentric circles. The crosses show the centre of mass of the bound pairs. In configuration (a), we have a correlation between an operator corresponding to the first four eigenvalues and an operator corresponding to the second four eigenvalues in clusters A and B, respectively. In contrast, configuration (b) shows a correlation between operators corresponding to the largest eigenvalue only and configuration (c) shows a correlation between operators corresponding to the second eigenvalue only.

B (residing at rungs $(x', x'+1)$) are the same as for cluster A (residing at rungs $(x, x+1)$), but with mirrored rungs, i.e. an operator acting on rungs $(x, x+1)$ acts in the same fashion on rungs $(x'+1, x')$.

Looking more closely, the first four operators annihilate or create a particle on rungs $x+1$ or x', respectively, thereby breaking or regrouping bound pairs residing on $(x+1, x+2)$ or $(x'-1, x')$, respectively. The second set of four operators annihilates or creates a particle on rungs x or $x'+1$, thereby breaking or regrouping bound pairs residing on rungs $(x, x+1)$ or $(x', x'+1)$. For a given odd separation $x'-x$, the combination of $x+1$ with x' requires the smallest number of pairs to be present in between the two clusters. The alternative combination is x with $x'+1$, which requires an additional pair in between (see figure 8). We could estimate

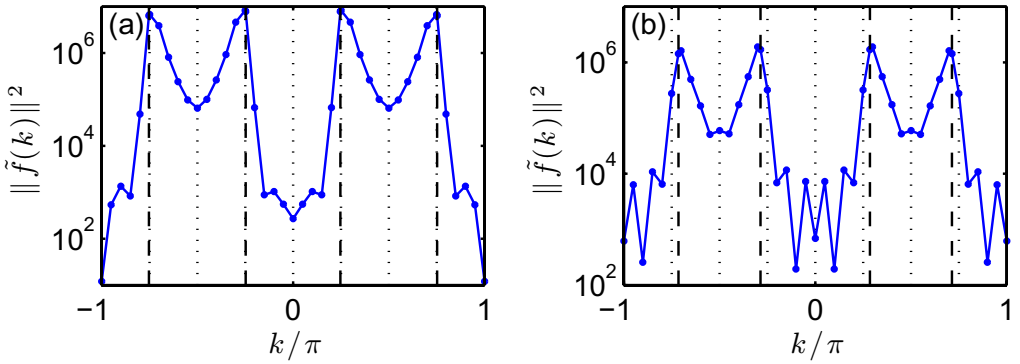

Figure 9. Fourier transform of the f-matrix obtained similarly to figure 5, for 1P correlations based on the four operators per cluster for a filling of (a) $\nu = 0.248$ and (b) $\nu = 0.286$. We find peaks at about $k = \pm k_\mathrm{F}$ and $k = \pm k_\mathrm{F} + \pi$ (dashed black lines).

their weights since the relative probability of an extra pair is the factor associated with increasing the separation by two. Since the correlations decay roughly as $\sim 10^{-r}$ (see figure 10), we predict two orders of magnitude. Similarly, when $x' - x$ is even, we get a mixture of the first four and the second four operators (see figure 8). This explains the difference in the weights of the two operator sets.

Thus, it turns out that for the 1P correlations, a cluster size of one rung would have already been large enough to reveal the dominant correlations. We will hence use as DOB:

$$\hat{O}^{A,\pm} = \mathbb{1}_x \otimes \frac{1}{\sqrt{2}} \left(\hat{c}_{\uparrow,x+1} \pm \hat{c}_{\downarrow,x+1} \right), \tag{7.8a}$$

$$\hat{O}^{B,\pm} = \frac{1}{\sqrt{2}} \left(\hat{c}_{\uparrow,x} \pm \hat{c}_{\downarrow,x} \right) \otimes \mathbb{1}_{x+1}, \tag{7.8b}$$

together with their Hermitian conjugates. (The fact that our operator basis consists only of operators acting on a single rung implies that it would have been sufficient to use single-rung clusters. However, for the sake of consistency with the rest of our analysis, we retain two-rung clusters here, too.)

The f-matrix based on these four operators (per cluster) is diagonal with equal entries for a given distance r. Its Fourier transform (see figure 9) gives a result distinct from the Fourier transform for CD and 2P correlations. The dominant wave vectors are $k = \pm k_\mathrm{F}$ and $k = \pi \pm k_\mathrm{F}$, where the latter is the product of an oscillation with $k = \pi$ and an oscillation with $k = \pm k_\mathrm{F}$. In total, we have an oscillation in the correlations of the form $(1 + (-1)^r)\mathrm{e}^{\pm \mathrm{i} k_\mathrm{F} r}$, i.e. an oscillation with $k = \pm k_\mathrm{F}$, and every second term being close to zero. The dominant wave vector $k = \pm k_\mathrm{F}$ is consistent with the usual behaviour of 1P Green's functions.

The reason for every second term being essentially zero is that the dominant hopping in the system, the correlated hopping, always changes the position of a particle by two rungs, so every second position is omitted. The small but finite value for hopping onto intermediate rungs is related to the finite $t_\parallel / t_\mathrm{c} = 10^{-2}$ that we use. It results in a second oscillation at $k = \pm k_\mathrm{F}$ located at intermediate rungs, whose relative strength compared with the dominant one is about 10^{-2}, which is consistent with the ratio $t_\parallel / t_\mathrm{c}$ that we used (see figure 10).

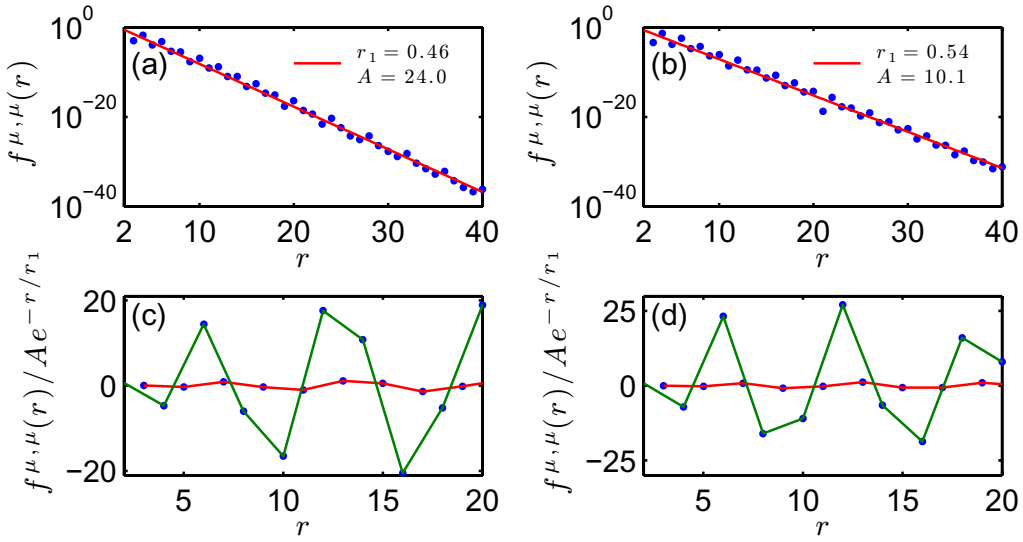

Figure 10. The 1P correlations for a filling of ((a) and (c)) $\nu = 0.248$ and ((b) and (d)) $\nu = 0.286$. ((a) and (b)) The 1P correlations (blue symbols) together with a fit of the form Ae^{-r/r_1} (red line). (b) and (d) The rescaled correlator $f^{\mu,\mu}(r)/Ae^{-r/r_1}$ (blue symbols) for distances up to $r = 20$. (Larger distances are omitted, because for them $f^{\mu,\mu}(r) < 10^{-16}$, which is the maximal computer precision.) One can see a strong oscillation (green curve) and a weak oscillation (red curve).

We fit the one independent f-matrix element $f^{\mu,\mu}$ to an exponential decay of the form Ae^{-r/r_1} (see figure 10), but apart from this we were not able to fit the exact functional dependence on r, especially the oscillations with $k = \pm k_F$. The reason for this is the existence of two oscillations where one is zero on every second rung, and that the data range for which reasonable 1P correlations are still present is too small and thus makes it susceptible to numerical noise. This can be seen already in the Fourier spectrum, where we find relatively broad peaks, as a result of the influence of the exponential envelope and the relatively short distance range available.

7.3. Two-particle correlations

The operator subspace for 2P ($\Delta N = 2$), in a cluster including two rungs, has the comparatively small dimension of four due to the infinite nearest-neighbour repulsion (see figure 2). These are $\hat{c}_{\uparrow,x}\hat{c}_{\downarrow,x+1}$, $\hat{c}_{\downarrow,x}\hat{c}_{\uparrow,x+1}$ and their Hermitian conjugates. In the present case of dominating t_c, these operators represent the creation and annihilation operators of bound pairs [2]. The operator analysis yields exactly the same four operators with degenerate weight for all distance regimes for both clusters A and B. The four operators are $1/\sqrt{2}(\hat{c}_{\uparrow,x}\hat{c}_{\downarrow,x+1} \pm \hat{c}_{\downarrow,x}\hat{c}_{\uparrow,x+1})$ together with their Hermitian conjugates, and they already represent the symmetric and antisymmetric combinations of the operators mentioned above.

The f-matrix (5.7) is diagonal in the basis of the four operators, with equal strength of correlations for a fixed distance apart from a possible sign. This may be expected, given the similar structure of the operators.

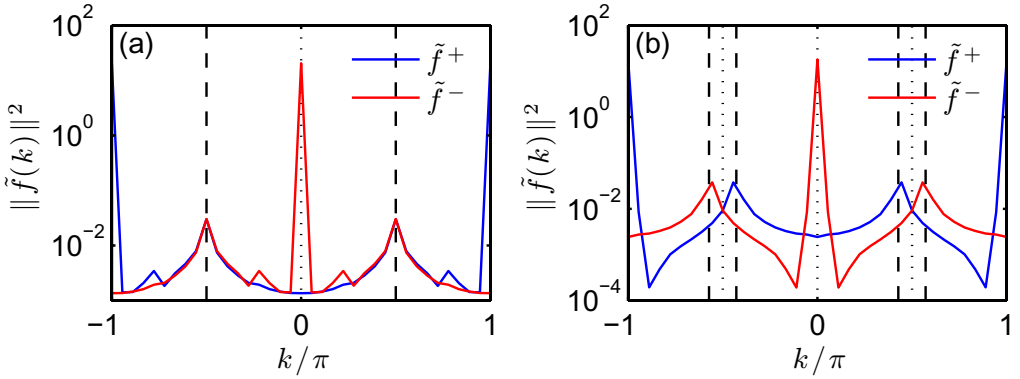

Figure 11. Fourier transform of the f-matrix for 2P correlations based on the operators chosen from the four-dimensional operator space for a filling of (a) $\nu = 0.248$ and (b) $\nu = 0.286$. For a detailed description see figure 5.

As for the CD correlations ($\Delta N = 0$), we apply a Fourier transform on the f-matrix (see figure 11) to identify the dominant wave vectors. Again, we find two spectra of similar form but shifted by π with respect to each other. Consequently, we redefine f^+ to $e^{i\pi r} f^+$, the part of the f-matrix belonging to the symmetric operators. Thus, we obtain one leading peak at $k = 0$ and sub-leading peaks at $k = 2k_F$. Given the similarity of the structure of the Fourier spectrum to that of the CD correlations, we fit the elements of the f-matrix to the form (7.3), but now expect $\gamma_2' < \gamma_2$, since in the Fourier spectrum the peaks at $k = 0$ are sharper than those at $k = 2k_F$. Already at the level of the f-matrix elements, we find an overall leading decay with residual oscillations, whose relative magnitude becomes smaller at large distances (since $\gamma_2' < \gamma_2$). Since all matrix elements are the same after redefining f^+, it is sufficient to fit $|f^{\mu,\mu}|$ for a given μ, which will have dominant k-vectors $k = 0$ and $k = \pm 2k_F$. The fit has errors of less than 5% throughout, with results as shown in figure 12. The overall behaviour is very similar to the one already found from the rms net correlations of this sector (see figure 4), up to the oscillatory part from the second term in (7.3). We see that the oscillations clearly decay more strongly than the actual strength $|f^{\mu,\mu}|$, in accord with $\gamma_2' < \gamma_2$.

In contrast to the CD correlations (see section 7.1.2), for the 2P correlations we do not find correlations that oscillate with phases shifted by $\Delta\phi = \pm\pi/2$. This may come from the fact that clusters with the size of two rungs have the minimal possible size to capture 2P correlations. The corresponding operator space has dimension four and the four possible operators are very similar in structure. We expect that for larger clusters and hence a larger operator space, we would find correlations, which also oscillate out of phase such that their oscillations cancel in the rms net correlations, in accord with (2.2).

8. Comparison to previous results

We are now ready to compare our CDM-based results with those obtained in [2] (see section IV.B therein) by Cheong and Henley (CH) from fitting simple correlation functions. The latter were computed exactly in [2] for accessible separations (up to 18 lattice sites) after mapping the large t_c model onto a hard-core bosonic system, evaluating the correlators numerically using a so-called interparticle expansion, and fitting the numerical results to simple functional forms in order to determine their leading and sub-leading r-dependences.

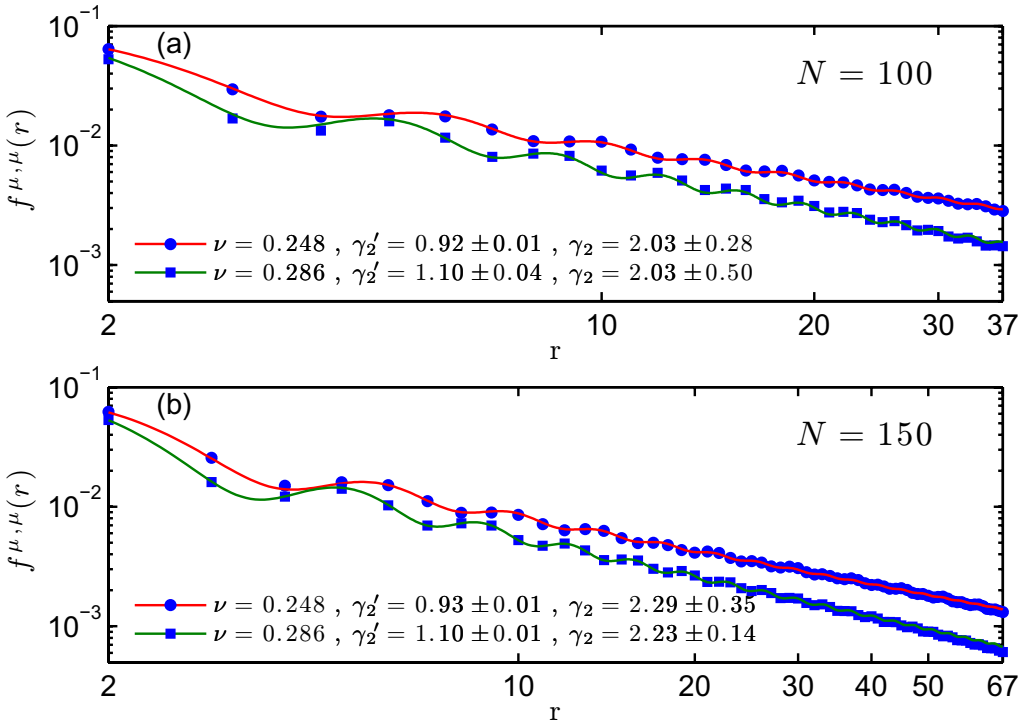

Figure 12. Fitting the 2P correlations to the form in (7.3) for a filling of $\nu = 0.248$ and 0.286 for a chain length of (a) $N = 100$ and (b) $N = 150$. The single points (blue circles and squares) are data points from the f-matrix and the lines (red and green) are the result of the fitting. The error of the exponents is calculated according to (6.1). Results in panels (a) and (b) were obtained from ground states calculated by retaining all contributions to bond singular spectra larger than 10^{-6} and 10^{-8}, respectively, which required maximal Hilbert space dimensions of $D \lesssim 200$ or $D \lesssim 500$, respectively. The increase in accuracy for (b) was needed to obtain good power-law behaviour out to distances about twice as large in (a). (The power laws turn to exponential decays beyond $r \simeq 37$ or 67 in (a) and (b), respectively, for reasons explained in section 4.2.) Since the exponents determined from (a) and (b) agree within the stated error margins, we conclude that the exponents for the power-law decay are converged with respect to the thermodynamic limit. Hence we used and deemed sufficient the accuracy chosen in (a) for all other results reported in this paper.

Overall, our results for the Hamiltonian (3.1) in the strongly correlated hopping regime agree qualitatively with [2], in that (i) 2P correlations and CD correlations show power-law behaviour, (ii) for the fillings we investigated, 2P correlations dominate at large distances, (iii) 1P correlations decay exponentially and are negligible over all distances except very short distances and (iv) the dominant and sub-dominant wave vectors are, respectively, $2k_F$ and 0 for the CD sector and 0 and $2k_F$ for the 2P sector.

However, our results for the power-law exponents γ_0 and γ_2 characterizing the decay of the dominant correlations in the CD and 2P sectors, respectively, are not in quantitative agreement with the exponents found by CH in [2] for CD and 2P correlators. Figure 13 compares the

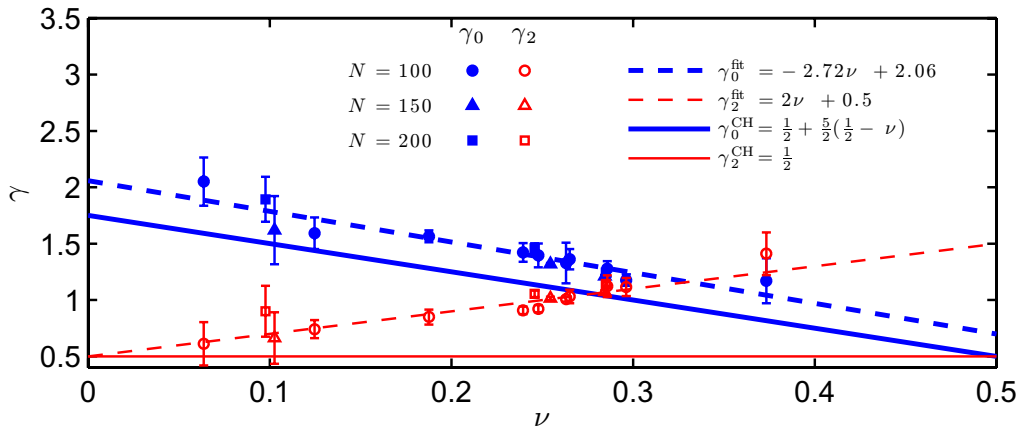

Figure 13. The power-law exponents for CD correlations (γ_0, filled symbols) and 2P correlations (γ_2, open symbols) obtained from the fitting in (7.3) for several fillings ν. We used chain lengths of $N = 100$ (circles), $N = 150$ (triangles) and $N = 200$ (squares). The errors of the exponents are defined as in (6.1) and are smallest for fillings around quarter filling. The reason for the somewhat larger errors in the CD exponent at small fillings is that there the wave length of Friedel-like oscillations caused by the boundaries (see section 6.2) becomes significant in comparison to the system sizes we are considering. The thick and thin dashed lines are linear fits to our numerical data for γ_0 and γ_2, respectively. The thick and thin solid lines show the corresponding predictions of CH [2].

filling-dependence of our exponents γ_0 and γ_2 obtained from (7.3) with that predicted by CH [2]. Such a direct comparison is justified, since in both symmetry sectors, CD and 2P, the correlation functions considered by CH can be written as linear combinations of the f-matrix elements studied by us (for which equation (7.5) yields a good simultaneous fit, as shown in figure 6). Indeed, for the 2P sector, the linear combination is trivial, since the pair operator $\Delta_{j,g} = 1/\sqrt{2}(\hat{c}_{\uparrow x}\hat{c}_{\downarrow x+1} + \hat{c}_{\downarrow x}\hat{c}_{\uparrow x+1})$ appearing in CH's (4.4) is one of the basis elements of our DOB. For the CD sector, the number operator $\hat{N}_x$ occurring in $\langle \hat{N}_x \hat{N}_{x+r} \rangle$ of CH's (4.7) can be expressed as a linear combination of the DOB elements given in our (7.1) and (7.2):

$$\hat{N}_x = \hat{n}_{\uparrow x}\hat{n}_{\downarrow x+1} = \tfrac{1}{\sqrt{3}}\hat{O}^1 + \tfrac{1}{\sqrt{42}}\hat{O}^3 + \tfrac{1}{\sqrt{2}}\hat{O}^6 + \tfrac{1}{\sqrt{7}}\mathbb{1}_x \otimes \mathbb{1}_{x+1}. \tag{8.1}$$

(The cluster identity operator $\mathbb{1}_x \otimes \mathbb{1}_{x+1}$ does not contribute to the CDM, due to the subtractions in (1.1) and (1.2).)

Consider first the exponent γ_0 for the CD correlations. CH [2] suggested it to depend on filling ν according to $\gamma_0^{\mathrm{CH}} = (1/2) + (5/2)((1/2) - \nu)$ (figure 13, thick solid line). While our result for γ_0 (figure 13, thick dashed line) likewise decreases linearly with ν, the magnitude of its slope and its offset are larger than those of CH (slope: -2.72 versus -2.5; offset: 2.06 versus 1.75, respectively).

For the dominant 2P correlations, CH predicted a constant power-law exponent of $\gamma_2^{\mathrm{CH}} = 1/2$ independent of filling (figure 13, thin solid line), coming from a universal correlation exponent for a chain of tightly bound spinless fermion pairs [10]. In contrast, our data imply a linear ν-dependence (figure 13, thin dashed line), going from $1/2$ at $\nu = 0$ to $3/2$ at $\nu = (1/2)$.

(Such a crossover was asserted by CH for a sub-leading contribution, without giving an explicit functional dependence on ν.)

In light of the discrepancies between our results and those of CH [2], two comments are in order. Firstly, we do not believe that they stem from finite-size or boundary effects, since these hardly affect our results; this is illustrated, for example, by the fact that the exponents extracted for $N = 100$ and 150 (figures 6 and 12) or for $N = 100$, 150 and 200 (figure 13) are essentially independent of N (they differ by at most a few per cent, which is within the margin of error of our fitting procedure).

Secondly, we note that the maximum distance studied by CH in [2], namely $r_{\max} = 18$, is significantly smaller than in our case, where $r_{\max} = 40$ for N ranging over 100, 150 and 200. We speculate that this is the main reason for the discrepancies—it is rather difficult to extract from numerical data an accurate power law for distances ranging only up to 18, in particular in the presence of superimposed oscillations, such as those depicted in figures 7 and 12. In figure 12, for example, the difference in the power-law decays depicted for two different fillings (circles and squares) becomes unambiguously evident only in the regime of largest distances shown, say between 25 and 37.

We conclude with some comments about the exponents in the limit of large fillings ($\nu \to 0.5$). By linear extrapolation of the behaviour shown in figure 13 for smaller fillings, we conjecture that for fillings larger than $\sim$0.35, eventually the CD correlations dominate over 2P correlations (see figure 13). This conclusion has also been found in [11], which similarly addresses diatomic real space pairing in the context of superconductivity. Their discussion, however, is not specifically constrained to one-dimensional systems, and one may wonder how the specific choice of parameters compares.

As the filling approaches 0.5 in an excluded-fermion chain, it is appropriate to think of the degrees of freedom as impurity states or holes in the crystalline matrix of pairs [11]. Then the natural length scale is the spacing between holes. The longer that spacing gets (it diverges as $\nu \to 0.5$), the larger also the system under investigation must be in order to reach the asymptotic limit. In other words, to see proper scaling behaviour in a uniform way, the system size should increase proportional to $1/(0.5 - \nu)$. In our case, the data became unreliable for $\nu \gtrsim 0.4$ (see figure 13); hence we cannot make definite statements about that regime. (For $\nu < 0.4$ however, we are confident that the data in figure 13 are essentially independent of system size, as emphasized above.)

9. Conclusions

In summary, we demonstrated that the DOB method for analysing the CDM is a useful tool to detect dominant correlations in a quantum lattice system. Starting from a ground state calculated with DMRG, we extracted all the important correlations present in our model system. Our proposed DOB method, firstly, determines a distance-independent basis of dominant operators on each cluster that carry the dominant correlations of the system, and secondly, encodes the distance dependence of the correlations in the f-matrix, the correlation matrix of the DOB operators. The f-matrix is then analysed in terms of decaying and oscillatory terms to extract the long-range behaviour of the correlations.

Overall, DMRG is a suitable method to calculate the CDM. The latter is easily and efficiently calculated within the framework of the MPS. The explicit breaking of (i) translational invariance by using finite system DMRG and (ii) a discrete symmetry of the model lead us to

develop certain strategies to restore these broken symmetries. The smoothing of the boundaries can still be further optimized or be replaced by periodic boundary conditions. However, we do not expect that this will have a significant influence on the conclusions drawn.

10. Outlook: larger cluster sizes

The size of clusters A and B is a limitation of the present implementation of the DOB method, as it constrains the analysis towards local operators. For some kinds of correlations however, larger clusters may be needed to capture the relevant physics [12]. Even for correlations approximately captured by a certain cluster size, the results may still show some dependence on the actual cluster size. For this purpose, an alternative strategy, which we leave as an outlook, appears viable: instead of the pair of local clusters used in the present work, one could use two 'super clusters' representing large contiguous parts of the system, including the left and right boundaries respectively.

Since MPS technology can be used to construct orthonormal effective basis sets to describe the left and right parts of the chain with respect to any specified site (as described in section A.2), it should also be possible to use these basis sets to obtain an efficient description of both super clusters (this is illustrated in figure A.9(c)). To be specific, let cluster A be the set of sites $1, \ldots, x$ ('left' cluster), while cluster B is the set of sites $x', \ldots, N$ ('right' cluster) with $x' - x = r > 0$. (The cluster sizes, x and $N - x' + 1$, should be similar; they should also be chosen rather large, to ensure that boundary effects at the very ends of the chains do not contaminate the analysis.) The MPS formulation of DMRG provides an effective set of basis states, $|l_{x+1}\rangle$ and $|r_{x'-1}\rangle$ (see section A.2 for details, in particular figure A.1), that can be used to construct an economical description of the left and right super clusters, respectively (as illustrated in figure A.9(c)). The CDM can then be defined with respect to these effective MPS basis states. A DOB analysis of such a CDM would then yield operator sets $\hat{O}^{A,\mu}$ and $\hat{O}^{B,\mu}$ acting on the system to the left of site $x+1$ and to the right of site $x'-1$, respectively (i.e. each $\hat{O}^{A,\mu}$ or $\hat{O}^{B,\mu}$ is a linear operator on the set of basis states $|l_{x+1}\rangle$ or $|r_{x'-1}\rangle$, respectively). Using the MPS in these parts as maps to the local Hilbert spaces, the action of these operators can be investigated on individual sites, thus determining the actual range of the dominant operator correlations without bias to some predetermined cluster size.

Acknowledgments

We thank S-A Cheong and A Läuchli for discussions and comments on the paper. This work was supported by DFG (SFB 631, SFB-TR 12, De-730/4-1 and De-730/4-2), Center for NanoScience (CENS; LMU) and Nanosystems Initiative Munich (NIM). CLH acknowledges the NSF for support through grant number DMR-0552461. This research was partially supported by the NSF under grant no. NSF PHY05-51164. JvD acknowledges the hospitality of the Kavli Institute for Theoretical Physics, UCSB, and of the Institute for Nuclear Theory, University of Washington, Seattle.

Appendix. The variational MPS approach

This appendix offers a tutorial introduction to the variational formulation of DMRG for finding the ground state of a one-dimensional quantum lattice model, based on MPS. It also explains how this approach can be used to efficiently calculate the CDM. We point out all the important properties of the MPS and explain how to perform basic quantum calculations such as evaluating scalar products and expectation values, as well as determining the action of local operators on the MPS and constructing a reduced density matrix. We explain how a given MPS can be optimized in an iterative fashion to find an excellent approximation for the global ground state. We also indicate briefly how the efficiency of the method can be enhanced by using Abelian symmetries.

We would like to emphasize that we make no attempt below at a complete historical overview of the DMRG approach or at a complete set of references, since numerous detailed expositions of this approach already exist in the literature (see the excellent review by Schollwöck [5]). Our aim is much more modest, namely to describe the strategy implemented in our code in enough detail to be understandable for interested non-experts.

A.1. Introduction

Quantum many-body systems deal with very large Hilbert spaces even for relatively small system sizes. For example, a one-dimensional quantum chain of N spin-$\frac{1}{2}$ particles forms a Hilbert space of dimension 2^N, which is exponential in system size. For quantum lattice models in 1D a very efficient numerical method is the DMRG, introduced by Steven R White [3, 4]. The problem of large Hilbert space dimension is avoided by an efficient description of the ground state, which discards those parts of the Hilbert space that have negligible weight in the ground state. In this manner, the state space dimension of the effective description becomes tractable, and it has been shown that this produces excellent results in many quasi one-dimensional systems. In the meantime, the method has been extended to time dependence, and various time-dependent Hamiltonians have been studied [13]–[16].

The original DMRG formulation did not rely on MPS but used 'block states' to represent the effective Hilbert spaces of one or more targeted states. The notion of MPS was introduced independently of DMRG [17]–[21] before it was realized that the algebraic structure of the ground state for one-dimensional systems calculated with DMRG can be described in terms of position-dependent MPS [6, 19], [22]–[27]. The MPS-based formulation of DMRG has proven to be very enlightening and fruitful, in particular the observation that DMRG is in essence a variational method [6] opened up rich connections to quantum information theory. A firmer theoretical grounding was based on the observation that the numerical effort depends strongly on the entanglement of the wavefunction [28]–[31]. Also some new fields of application arose like periodic systems [6] and finite temperature calculations through purification of the density operator [32, 33].

The origin of the MPS structure underlying the DMRG approach can be understood as follows (a detailed description will follow later): pick any specific site of the quantum lattice model, say site k, representing a local degree of freedom whose possible values are labelled by an index σ_k (e.g. for a chain of spinless fermions, $\sigma_k = 0$ or 1 would represent an empty or

occupied site). Any many-body state $|\psi\rangle$ of the full chain can be expressed in the form

$$|\psi\rangle = \sum_{l_k r_k \sigma_k} A^{[\sigma_k]}_{l_k r_k} |l_k\rangle\, |\sigma_k\rangle\, |r_k\rangle, \tag{A.1}$$

where $|l_k\rangle$ and $|r_k\rangle$ are sets of states (say N_l and N_r in number) describing the parts of the chain to the left and right of the current site k, respectively, and for each σ_k, $A^{[\sigma_k]}$ is a matrix with matrix elements $A^{[\sigma_k]}_{l_k r_k}$ and dimension $N_l \times N_r$. Since such a description is possible for any site k, the state $|\psi\rangle$ can be specified in terms of the set of all matrices $A^{[\sigma_k]}$, resulting in an MPS of the form

$$|\psi\rangle = \sum_{\sigma_1 \ldots \sigma_N} \left(A^{[\sigma_1]} \ldots A^{[\sigma_N]}\right)_{l_1 r_N} |\sigma_1\rangle \ldots |\sigma_N\rangle. \tag{A.2}$$

One may now seek to minimize the ground state energy within the space of all MPS, treating the matrix elements of the A-matrices as variational parameters to minimize the expectation value $\langle\psi|H|\psi\rangle$. If this is done by sequentially stepping through all matrices in the MPS and optimizing one matrix at a time (while keeping the other matrices fixed), the resulting procedure is equivalent to a strictly variational minimization of the ground state energy within the space of all MPS of the form (A.2) [6, 19, 23, 25, 26]. If instead the optimization is performed for two adjacent matrices at a time, the resulting (quasi-variational) procedure is equivalent to White's original formulation of DMRG [6, 19, 23, 25, 26].

In general, such an approach works for both bosonic and fermionic systems. However, to be efficient the method needs a local Hilbert space with finite and small dimension, limiting its applicability to cases where the local Hilbert space is finite dimensional *a priori* (e.g. fermions or hard-core bosons) or effectively reduced to a finite dimension, e.g. by interactions. For example, such a reduction is possible if there is a large repulsion between bosons on the same site such that only a few states with small occupation number will actually take part in the ground state. For fermions, on the other hand, the fermionic sign must be properly taken care of. The anti-commutation rules of fermionic creation and annihilation operators cause the action of an operator on a single site to be non-local because the occupations of the other sites have to be accounted for. To simplify the problem, a Jordan–Wigner transformation [34] can be used to transform fermionic creation and annihilation operators to new operators that obey bosonic commutation relations for any two operators referring to different sites. This greatly simplifies the numerical treatment of these operators as fermionic signs can be (almost) ignored.

Before outlining in more detail the above-mentioned optimization scheme for determining the ground state (see section A.3), we present in section A.2 various technical ingredients needed when working with MPS.

A.2. MPSs

A.2.1. Construction of MPSs. We consider a chain with open boundary conditions consisting of N equal sites with a local Hilbert space dimension of d. A state $|\psi\rangle$ is described by

$$|\psi\rangle = \sum_{\sigma_1 \ldots \sigma_N} \psi_{\sigma_1, \ldots, \sigma_N} |\sigma_1\rangle \ldots |\sigma_N\rangle, \tag{A.3}$$

where $\sigma_i = 1, \ldots, d$ labels the local basis states of site i. In general, the size of the coefficient space ψ scales with $\mathcal{O}(d^N)$. This can be rewritten in a matrix decomposition of the form

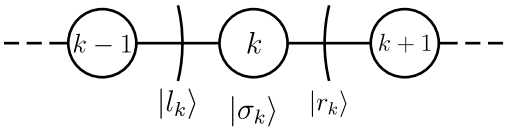

Figure A.1. The current site with effective basis sets.

(A.2) with a set of N times d matrices $A^{[\sigma_k]}$ (see section A.2.3 for details). Formally, this decomposition has two open indices, namely the first index of $A^{[\sigma_1]}$ and the second index of $A^{[\sigma_N]}$, as $A^{[\sigma_1]}$ and $A^{[\sigma_N]}$ are not multiplied onto a matrix to the left and the right, respectively. For periodic boundary conditions these two indices would be connected by a trace over the matrix decomposition, giving a scalar. In the case of open boundary conditions, the two indices range only over one value (see section A.2.3), i.e. the matrix decomposition is a 1×1 matrix, which is a scalar.

If these A-matrices are sufficiently large this decomposition is formally exact, but since that would require A-matrices of exponentially large size, such an exact description is only of academic interest. The reason why the A-matrices are introduced is that they offer a very intuitive strategy for reducing the numerical resources needed to describe a given quantum state. This strategy involves limiting the dimensions of these matrices by systematically using SVD and retaining only the set of largest singular values. The A-matrices can be chosen much smaller while still giving a very good approximation of the state $|\psi\rangle$.

Selecting a certain site k, the state can be rewritten in the form (A.1). The effective 'left' basis $|l_k\rangle = \sum_{\sigma_1 \ldots \sigma_{k-1}} A^{[\sigma_1]} \ldots A^{[\sigma_{k-1}]} |\sigma_1\rangle \ldots |\sigma_{k-1}\rangle$ describes the sites $j = 1, \ldots, k-1$; the effective 'right' basis $|r_k\rangle$ similarly describes the sites $j = k+1, \ldots, N$. Site k is called the *current* site, as the description of the state makes explicit only the A-matrix of this site (see figure A.1).

So far (A.3) and (A.1) are equivalent, but now we have a representation of the state that allows a convenient truncation of the total Hilbert space, used for the description of an MPS. For example, if we introduce a parameter D and truncate all effective Hilbert spaces of all sites to the dimension D, each $A^{[\sigma_k]}$-matrix has at most the dimension $D \times D$. This reduces the resources used to describe a state from $\mathcal{O}(d^N)$ for the full many-body Hilbert space down to $\mathcal{O}(ND^2d)$. This is linear in the system size, assuming that the size required for D to accurately describe the state grows significantly slower than linearly in N. This, in fact, turns out to be the case for ground state calculations [35]. Details of this truncation procedure and estimates of the resulting error are described in section A.2.5.

A.2.2. Global view and local view. MPSs can be viewed in two alternative ways: a global view and a local view. Both views are equivalent and both have their applications. In the global view the state is expressed as in (A.2), i.e. the effective Hilbert spaces have been used 'only' to reduce resources. The state is stored in the A-matrices, but the effective basis sets will be contracted out. This perception has to be handled very carefully, because contracting out the effective basis sets leads to higher costs in resources! In the local view the state is expressed as in (A.1). It is called local because there is one special site, the *current* site, and all other sites are combined in effective orthonormalized basis sets. Usually, the local view is used iteratively for every site. In this perception, we need effective descriptions of operators contributing to the Hamiltonian acting on other sites than the current site (see section A.2.8).

A.2.3. Details of the A-matrices. The A-matrices have some useful properties that hold independently of the truncation scheme used to limit the effective Hilbert spaces. First of all, we note that by construction $\dim(\mathcal{H}^{r_{k-1}}) \equiv \dim(\mathcal{H}^{l_k})$; otherwise the matrix products in (A.2) would be ill-defined. Based on this, we can find another interpretation of the A-matrices in the local view. The part of the chain to the left of site k (where k is far from the ends for simplicity) is described by the effective basis $|l_k\rangle$, which is built of truncated A-matrices:

$$\begin{aligned}
|l_k\rangle &= \sum_{\sigma_1,\ldots,\sigma_{k-1}} \left(A^{[\sigma_1]}\ldots A^{[\sigma_{k-1}]}\right)_{1l_k} |\sigma_1\rangle\ldots|\sigma_{k-1}\rangle \\
&= \sum_{\sigma_{k-1}}\sum_{l_{k-1}} \underbrace{\sum_{\sigma_1,\ldots,\sigma_{k-2}} \left(A^{[\sigma_1]}\ldots A^{[\sigma_{k-2}]}\right)_{1l_{k-1}} |\sigma_1\rangle\ldots|\sigma_{k-2}\rangle}_{|l_{k-1}\rangle} A^{[\sigma_{k-1}]}_{l_{k-1},l_k} |\sigma_{k-1}\rangle \\
&= \sum_{\sigma_{k-1},l_{k-1}} A^{[\sigma_{k-1}]}_{l_{k-1}l_k} |l_{k-1}\rangle\,|\sigma_{k-1}\rangle. \qquad \text{(A.4)}
\end{aligned}$$

The $A^{[\sigma_{k-1}]}$-matrix maps the effective left basis $|l_{k-1}\rangle$ together with the local $|\sigma_{k-1}\rangle$ basis onto the effective left basis $|l_k\rangle$! The same argument applied on the effective right basis of site k leads to the transformation of $|r_{k+1}\rangle$ and $|\sigma_{k+1}\rangle$ into $|r_k\rangle$ via the $A^{[\sigma_{k+1}]}$-matrix:

$$|r_k\rangle = \sum_{\sigma_{k+1},r_{k+1}} A^{[\sigma_{k+1}]}_{r_k r_{k+1}} |\sigma_{k+1}\rangle\,|r_{k+1}\rangle. \qquad \text{(A.5)}$$

So far, this may be any transformation, but in order to deal with properly orthonormal basis sets, we may impose unitarity on the transformation (see below).

The A-matrices towards the ends of the chain have to be discussed separately. The use of open boundary conditions implies that we have a one-dimensional effective state space to the left of site 1 and the right of site N, respectively, both representing the empty state. This implies that $\dim(\mathcal{H}^{l_1}) = 1 = \dim(\mathcal{H}^{r_N})$. Moving inwards from the ends of the chain, the effective Hilbert spaces acquire dimension $d^1, d^2, \ldots$ until they become larger than D and need to be truncated. Correspondingly, the dimension of matrix $A^{[\sigma_k]}$ is $D_{k-1} \times D_k$, where $D_k = \min(d^k, d^{N-k}, D)$. There is no truncation needed if $\dim(\mathcal{H}^{l_k}) * d = \dim(\mathcal{H}^{r_k})$ or $\dim(\mathcal{H}^{r_k}) * d = \dim(\mathcal{H}^{l_k})$. In these cases we simply choose $A_{(l_k\sigma_k)r_k} = \mathbb{1}$ and $A_{l_k(r_k\sigma_k)} = \mathbb{1}$, respectively.

Summarizing, the A-matrices have two functions. If site i is the current site in (A.1), the $A^{[\sigma_i]}$-matrices represent the state, i.e. its coefficients specify the linear combination of basis states $|l_k\rangle$, $|\sigma_k\rangle$ and $|r_k\rangle$. On the other hand, if not the current site, the A-matrices are used as a mapping to build the effective orthonormal basis for the current site, as we describe next:

Orthonormal basis sets. In the local view, the whole system is described by the A-matrices of the current site k in the effective left basis, the effective right basis and the local basis of site k. *A priori*, the basis states form an orthonormal set only for the local basis set, but we may ask for the effective basis sets $|l\rangle$ and $|r\rangle$[4] to be orthonormal, too, i.e. require them to obey:

$$\begin{aligned}
\langle l'|l\rangle &= \delta_{l'l}, \\
\langle r'|r\rangle &= \delta_{r'r}.
\end{aligned} \qquad \text{(A.6)}$$

[4] From now on, the index k is only displayed when several sites are involved. For the current site or in the case when only one A-matrix is considered, the index will be dropped.

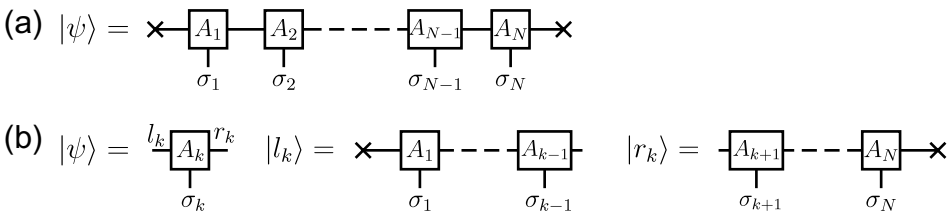

Figure A.2. Graphical representation of an MPS in (a) the global view and (b) the local view.

This immediately implies the following condition on the $A^{[\sigma_j]}$-matrices, using (A.4) and (A.5) (for a derivation, see section A.5.1):

$$\begin{aligned} \sum_{\sigma_j} A^{[\sigma_j]^\dagger} A^{[\sigma_j]} &= \mathbb{1} \qquad \text{for } j < k, \\ \sum_{\sigma_j} A^{[\sigma_j]} A^{[\sigma_j]^\dagger} &= \mathbb{1} \qquad \text{for } j > k. \end{aligned} \tag{A.7}$$

The orthonormality (A.6) for both the left and right basis states holds only for the current site. For the other sites there is always only one orthonormal effective basis.

Graphical representation. MPSs can be depicted in a convenient graphical representation (see figure A.2). In this representation, A-matrices are displayed as boxes and $A^{[\sigma_k]}$ is replaced by A_k for brevity. Indices correspond to links from the boxes. The left link connects to the effective left basis, the right link to the right one, and the link at the bottom to the local basis. Sometimes indices are explicitly written on the links to emphasize the structure of the sketch. Connected links denote a summation over the indices (also called contraction) of the corresponding $A^{[\sigma]}$-matrices. At the boundaries of the chain, a cross is used to indicate the vacuum state.

A.2.4. Orthonormalization of effective basis states. We now describe how an arbitrary MPS state can be rewritten into a form where its local view with respect to a given site has orthonormal left and right basis states. It should be emphasized that this really just amounts to a reshuffling of information among the state's A-matrices without changing the state itself, by exploiting the freedom that we can always insert any $X^{-1}X = \mathbb{1}$ at any position in the MPS without altering it.

Assume site k to be the current site and assume that it has an orthonormal left basis (the latter is automatically fulfilled for $k = 1$). We need a procedure to ensure that when the current site is switched to site $k+1$, this site, too, will have an orthonormal left basis. (This is required for the orthonormality properties used in the proof in section A.5.1. A similar procedure can be used to ensure that site $k-1$ has an orthonormal right basis provided k has such a basis.) For this purpose we use the singular value decomposition (SVD; see section A.5.2) for which we have to rewrite $A^{[\sigma_k]}_{l_k r_k}$ by *fusing* the indices l_k and σ_k:

$$A^{[\sigma_k]}_{l_k r_k} \widehat{=} A_{(l_k \sigma_k) r_k} = \sum_{m,n} u_{(l_k \sigma_k) m} s_{mn} (v^\dagger)_{n r_k} \widehat{=} \sum_m u^{[\sigma_k]}_{l_k m} (s v^\dagger)_{m r_k}, \tag{A.8}$$

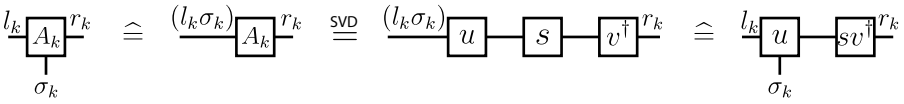

Figure A.3. SVD of the A-matrices.

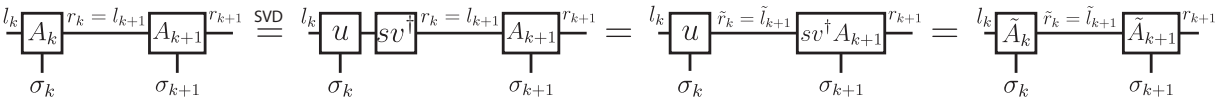

Figure A.4. Rearrangement of the A-matrices to switch the current site from site k to $k+1$.

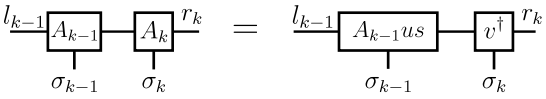

Figure A.5. Orthonormal effective right basis for site $k-1$.

where m, n and r_k have the same index range (see figure A.3). Specifically, u fulfills

$$\mathbb{1} = u^\dagger u = \sum_{(l_k\sigma_k)} u^*_{(l_k\sigma_k),m'} u_{(l_k\sigma_k),m}\,, \tag{A.9}$$

which is equivalent to the orthonormality condition (A.7) for the $A^{[\sigma_k]}$-matrices.

As u replaces $A^{[\sigma_k]}$ and $sv^\dagger$ is contracted onto $A^{[\sigma_{k+1}]}$, this leaves the overall state unchanged (for a graphical depiction see figure A.4):

$$\begin{aligned} A^{[\sigma_k]}A^{[\sigma_{k+1}]} &= \sum_{(r_k=l_{k+1})} A^{[\sigma_k]}_{l_k r_k} A^{[\sigma_{k+1}]}_{l_{k+1} r_{k+1}} = \sum_{(r_k=l_{k+1})} \sum_m u^{[\sigma_k]}_{l_k m} (sv^\dagger)_{m r_k} A^{[\sigma_{k+1}]}_{l_{k+1} r_{k+1}} \\ &= u^{[\sigma_k]} (sv^\dagger A_{k+1})^{[\sigma_{k+1}]} \equiv \tilde{A}^{[\sigma_k]} \tilde{A}^{[\sigma_{k+1}]}. \end{aligned} \tag{A.10}$$

Site $k+1$ now has an orthonormal effective left basis. A similar procedure works for the effective right basis, see figure A.5. To obtain an orthonormal effective left basis for the current site k, we start with the first site, update $A^{[\sigma_1]}$ and $A^{[\sigma_2]}$, move to the next site, update $A^{[\sigma_2]}$ and $A^{[\sigma_3]}$, and so on until site $k-1$. For an orthonormal effective right basis, we start from site N and apply an analogous procedure in the other direction.

If the state $|\psi\rangle$ is in the local description of site k with orthonormal basis sets $|l_k\rangle$, $|\sigma_k\rangle$ and $|r_k\rangle$, it is now very easy to change the current site to site $k \pm 1$, with corresponding new orthonormal basis sets $|l_{k\pm1}\rangle$, $|\sigma_{k\pm1}\rangle$ and $|r_{k\pm1}\rangle$. Suppose we want to change the current site from site k to site $k+1$. Following the procedure described above, site $k+1$ already has an orthonormal right basis and all the sites left of site k fulfill the orthonormality condition. All that is left to do is to update sites k and $k+1$ to obtain an orthonormal left basis for site $k+1$. This is called a *switch* of the current site from site k to site $k+1$. The switch from site k to site $k-1$ is done analogously.

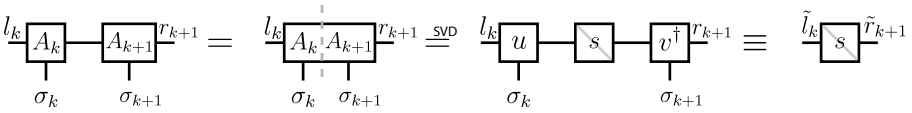

Figure A.6. Procedure for site update within two-site DMRG. The grey line through the s indicates that s is the diagonal matrix of singular values.

A.2.5. Hilbert space truncation. A central ingredient in the variational optimization of the ground state (see section A.3.1 below) is the truncation of the effective Hilbert spaces associated with a given A-matrix. The strategy for truncating the effective Hilbert spaces is completely analogous to the original DMRG formulation [25]. The DMRG truncation scheme is based on discarding that part of the Hilbert space on which a certain density matrix has sufficiently small weight. There are two ways to obtain an appropriate reduced density matrix: two-site DMRG [3]–[5] and one-site DMRG [5]. The crucial difference between the two is that one-site DMRG is strictly variational in the sense that the energy is monotonically decreasing with each step, whereas in two-site DMRG the energy may (slightly) increase in some steps, but with the advantage that the cutoff dimension can be chosen dynamically in each step.

Two-site DMRG. Two-site DMRG arises when variationally optimizing two sites at a time. We consider two current sites, say k and $k+1$, and we may choose the cutoff dimension site-dependent: $D \to D_k \equiv \dim(\mathcal{H}^{l_k})$. Following section A.2.4, we assume site k to have an orthonormal left basis and site $k+1$ to have an orthonormal right basis. After contracting the indices connecting $A^{[\sigma_k]}$ and $A^{[\sigma_{k+1}]}$ (see figure A.6), the state is described by $A^{[\sigma_k\sigma_{k+1}]}_{l_k r_{k+1}}$. In this description, we may optimize the ground state locally by variationally minimizing the ground state energy with respect to $A^{[\sigma_k\sigma_{k+1}]}_{l_k r_{k+1}}$ (see section A.3.1). Afterwards, we need to decompose $A^{[\sigma_k\sigma_{k+1}]}_{l_k r_{k+1}}$ into $A^{[\sigma_k]}$ and $A^{[\sigma_{k+1}]}$ again. This can be accomplished via SVD (see section A.5.2) by fusing the indices $l_k, \sigma_k \to (l_k\sigma_k)$ and $r_{k+1}, \sigma_{k+1} \to (r_{k+1}\sigma_{k+1})$ (see figure A.6) to obtain $A^{[\sigma_k\sigma_{k+1}]}_{l_k r_{k+1}} = \sum_i u^{[\sigma_k]}_{l_k i} s_i (v^\dagger)^{[\sigma_{k+1}]}_{i r_{k+1}}$, where $i = 1 \ldots \min(dD_k, dD_{k+2})$. Using the column unitarity of u and the row unitarity of $v^\dagger$ (see section A.5.2), we rewrite the state as

$$
\begin{aligned}
|\psi\rangle &= \sum_{l_k r_{k+1}\sigma_k\sigma_{k+1}} \left(\sum_i u^{[\sigma_k]}_{l_k i} s_i (v^\dagger)^{[\sigma_{k+1}]}_{i r_{k+1}} \right) |l_k\rangle\, |\sigma_k\rangle\, |\sigma_{k+1}\rangle\, |r_{k+1}\rangle \\
&= \sum_i s_i \underbrace{\left(\sum_{l_k\sigma_k} u^{[\sigma_k]}_{l_k i} |l_k\rangle\, |\sigma_k\rangle \right)}_{|\tilde{l}_i\rangle} \underbrace{\left(\sum_{r_{k+1}\sigma_{k+1}} (v^\dagger)^{[\sigma_{k+1}]}_{i r_{k+1}} |\sigma_{k+1}\rangle\, |r_{k+1}\rangle \right)}_{|\tilde{r}_i\rangle} \\
&= \sum_i s_i |\tilde{l}_i\rangle\, |\tilde{r}_i\rangle\,, \qquad \text{(A.11)}
\end{aligned}
$$

where the new set of basis states $|\tilde{l}_i\rangle$ and $|\tilde{r}_i\rangle$ is orthonormal with $\langle\tilde{l}_{i'}|\tilde{l}_i\rangle = \delta_{i'i}$ and $\langle\tilde{r}_{i'}|\tilde{r}_i\rangle = \delta_{i'i}$. This representation of the state may be seen as residing on the bond between k and $k+1$, with effective orthonormal basis sets for the parts of the system to the left and right of the bond. Reduced density matrices for these parts of the system, obtained by tracing out the respective

complementary part, have the form:

$$\rho^{[L]} = \sum_i s_i^2 |\tilde{l}_i\rangle\langle\tilde{l}_i|\,, \qquad \rho^{[R]} = \sum_i s_i^2\, |\tilde{r}_i\rangle\,\langle\tilde{r}_i|\,. \tag{A.12}$$

The standard DMRG truncation scheme amounts to truncating $\rho^{[L]}$ and $\rho^{[R]}$ according to their singular values s_i. We could either keep all singular values greater than a certain cutoff, thereby specifying a value for D_{k+1} between 1 and $\min(dD_k, dD_{k+2})$, or alternatively choose $D_k = D$ to be site independent for simplicity. This step makes the method not strictly variational, since we discard some part of the Hilbert space, which could increase the energy. It turns out that this potential increase of energy is negligible in practice. We can obtain a measure for the information lost due to truncation by using the von Neumann entropy $S = -\mathrm{tr}(\rho \ln \rho)$, given by

$$\varepsilon \equiv -\sum_{i>D} s_i^2 \ln(s_i^2), \tag{A.13}$$

where $\sum s_i^2 = 1$ due to the normalization of $|\psi\rangle$.

One-site DMRG. One-site DMRG arises when variationally optimizing one site at a time. In contrast to two-site DMRG, one-site DMRG does not easily allow for dynamical truncation during the calculation. (It is possible in principle to implement the latter, but if one decides to use dynamical truncation, it would be advisable to do so using two-site DMRG.) The truncation is fixed by the initial choice of D, but it is still possible to determine an estimate on the error of this truncation by analysing the reduced density matrix. Starting from an expression for the full density matrix in the local view (the current site k with orthonormal effective basis sets)

$$\begin{aligned}\rho = |\psi\rangle\langle\psi| &= \left(\sum_{lr\sigma} A_{lr}^{[\sigma]} |l\rangle|\sigma\rangle|r\rangle\right)\left(\sum_{l'r'\sigma'} A_{l'r'}^{[\sigma']*} \langle l'|\langle\sigma'|\langle r'|\right) \\ &= \sum_{lr\sigma l'r'\sigma'} A_{lr}^{[\sigma]} A_{l'r'}^{[\sigma']*} |l\rangle\langle l'||\sigma\rangle\langle\sigma'||r\rangle\langle r'|,\end{aligned} \tag{A.14}$$

we trace out the effective right basis and obtain a reduced density matrix for the current site and the left part of the system:

$$\rho^{[l_{k+1}]} = \sum_{lr\sigma l'\sigma'} A_{lr}^{[\sigma]} A_{l'r}^{[\sigma']*} |l\rangle\langle l'||\sigma\rangle\langle\sigma'|. \tag{A.15}$$

This reduced density matrix carries the label l_{k+1} because it corresponds precisely to the density matrix $|l_{k+1}\rangle\langle l'_{k+1}|$. So if we switch the current site from site k to site $k+1$, we can check the error of the truncation of $\mathcal{H}^{l_{k+1}}$. Fusing the indices l and σ, we obtain

$$\begin{aligned}\rho^{[l_{k+1}]} &= \sum_{lr\sigma l'\sigma'} A_{(l\sigma)r} A^*_{(l'\sigma')r} |(l\sigma)\rangle\langle(l'\sigma')| \\ &= \sum_{lr\sigma l'\sigma'} A_{(l\sigma)r} (A^\dagger)_{r(l'\sigma')} |(l\sigma)\rangle\langle(l'\sigma')| \\ &= \sum_{l\sigma l'\sigma'} (AA^\dagger)_{(l\sigma)(l'\sigma')} |(l\sigma)\rangle\langle(l'\sigma')|.\end{aligned} \tag{A.16}$$

We do not need to diagonalize the coefficient matrix $AA^\dagger$ to obtain the largest weights in the density matrix, because we obtain its eigenvalues as a byproduct of the following manipulations

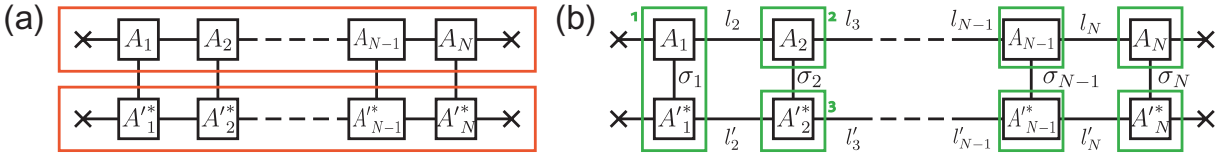

Figure A.7. Scalar product, computed in two different orders. (a) First, all A-matrices of $|\psi\rangle$ and $|\psi'\rangle$ are contracted and then contraction over the local indices is carried out. (b) First, for site 1, we contract over the local indices of A_1 and A'_1. Then we contract over the effective index between A_1 and A_2 and afterwards over the indices between the resulting object and $(A'_2)^*$. Proceeding over the whole chain yields the scalar product.

anyway [5]. To switch the current site we need to apply a SVD (see section A.2.4) and obtain $A = usv^\dagger$ (this is not the usual A-matrix, but the index-fused form). This directly yields $AA^\dagger = usv^\dagger vsu^\dagger = us^2u^\dagger$, which corresponds to the diagonalization of $\rho^{[l_{k+1}]}$, implying that the weights of the density matrix are equal to s^2. Of course this works also for the right effective basis. With such an expression, we can check whether the effective Hilbert space dimension D of $\mathcal{H}^{l_{k+1}}$ is too small or not. For example, we could ask for the smallest singular value s_D to be at least n orders of magnitude smaller than the largest one s_1, i.e. the respective weights in the density matrix would be $2n$ orders of magnitude apart. If the singular values do not decrease that rapidly, we have to choose a greater D.

A.2.6. Scalar product. The scalar product of two states $|\psi\rangle$ and $|\psi'\rangle$ is one of the simplest operations we can perform with MPSs. It is calculated most conveniently in the global view because then we do not need to care about orthonormalization of the A-matrices:

$$\begin{aligned}\langle\psi'|\psi\rangle &= \langle\sigma'_1|\ldots\langle\sigma'_N| \sum_{\sigma'_1\ldots\sigma'_N} (A'^{[\sigma'_1]}\ldots A'^{[\sigma'_N]})^* \sum_{\sigma_1\ldots\sigma_N} (A^{[\sigma_1]}\ldots A^{[\sigma_N]})\,|\sigma_1\rangle\ldots|\sigma_N\rangle \\ &= \sum_{\sigma_1\ldots\sigma_N} (A'^{[\sigma_1]}\ldots A'^{[\sigma_N]})^* (A^{[\sigma_1]}\ldots A^{[\sigma_N]}),\end{aligned} \tag{A.17}$$

using the orthonormality of the local basis $\langle\sigma'_k|\sigma_l\rangle = \delta_{kl}\delta_{\sigma'_k\sigma_k}$. In principle, the order in which these contractions are carried out is irrelevant, but in practice it is possible to choose an order in which this summation over the full Hilbert space is carried out very efficiently by exploiting the one-dimensional structure of the matrix product state (see figure A.7 for a graphical explanation). For details of the numerical costs, see section A.5.3. In method (a), after contracting all A-matrices of $|\psi\rangle$ and $|\psi'\rangle$, we have to perform a contraction over the full Hilbert space, i.e. a $1 \times d^N$ matrix is multiplied with a $d^N \times 1$ matrix. This contraction is of order $\mathcal{O}(d^N)$, which is completely unfeasible for practical purposes. In method (b), the most 'expensive' contraction is in the middle of the chain, say at site k, and it is of order $\mathcal{O}(dD^3)$. Here the A-matrices are viewed as three-index objects $A_{l_k r_k \sigma_k}$ with dimension $D \times D \times d$. All sites left of site k are represented by a $D \times D$ matrix, say $L^{l_k}_{l'_k}$. Contracting this with the matrix at site k yields the object $\sum_{l_k} L^{l_k}_{l'_k} A_{l_k r_k \sigma_k}$, which has dimensions $D \times D \times d$, and since the sum contains D terms, the overall cost is $\mathcal{O}(dD^3)$. Thus, in practice, method (b) is rather efficient and renders such calculations feasible in practice.

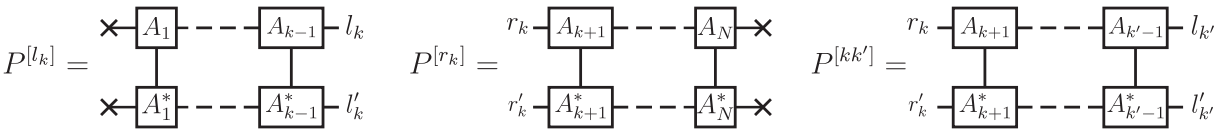

Figure A.8. Partial products associated with site k.

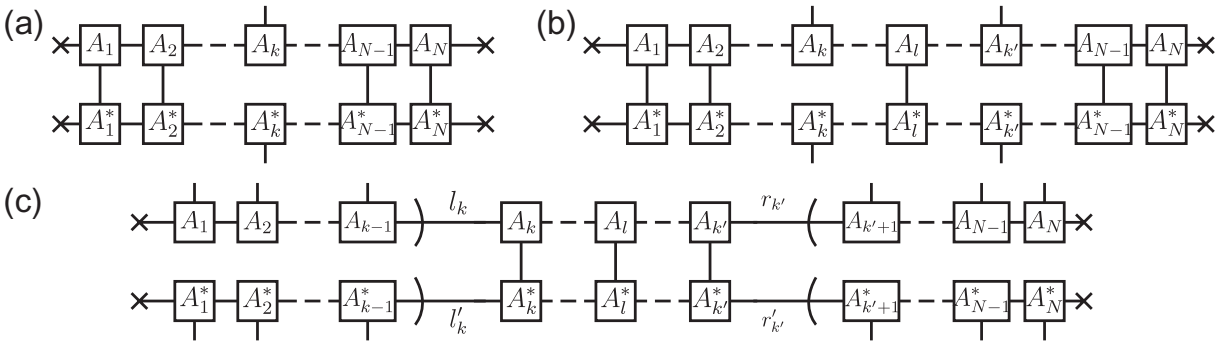

Figure A.9. Reduced density matrix (a) $\rho_{\{k\}}$ for site k, (b) $\rho_{\{kk'\}}$ for sites k and k', where $k < l < k'$, and (c) for two superclusters to the left of site k and the right of site k', respectively, which are described in terms of MPS basis states $|l_k\rangle$ and $|r_{k'}\rangle$, respectively, where $k < l < k'$.

Partial product. Sometimes it is required to calculate a product over only a part of the MPS. This is done the same way as the scalar product

$$(P^{[L_k]})_{l_k l'_k} \equiv \sum_{\sigma_1 \ldots \sigma_{k-1}} \left(A^{[\sigma_1]} \ldots A^{[\sigma_{k-1}]}\right)^*_{l'_k} \left(A^{[\sigma_1]} \ldots A^{[\sigma_{k-1}]}\right)_{l_k}, \tag{A.18}$$

$$(P^{[R_k]})_{r_k r'_k} \equiv \sum_{\sigma_{k+1} \ldots \sigma_N} \left(A^{[\sigma_{k+1}]} \ldots A^{[\sigma_N]}\right)^*_{r'_k} \left(A^{[\sigma_{k+1}]} \ldots A^{[\sigma_N]}\right)_{r_k}, \tag{A.19}$$

$$(P^{[kk']})_{r_k r'_k, l_{k'} l'_{k'}} \equiv \sum_{\sigma_{k+1} \ldots \sigma_{k'-1}} \left(A^{[\sigma_{k+1}]} \ldots A^{[\sigma_{k'-1}]}\right)^*_{r'_k\, l'_{k'}} \left(A^{[\sigma_{k+1}]} \ldots A^{[\sigma_{k'-1}]}\right)_{r_k\, l_{k'}}. \tag{A.20}$$

Note that $P^{[L_k]}$ and $P^{[R_k]}$ are matrices in the indices l_k and r_k, respectively (see figure A.8). In fact, they correspond to the overlap matrices $\langle l'_k | l_k \rangle$ and $\langle r'_k | r_k \rangle$, respectively.

A.2.7. Reduced density matrix. The pure density matrix given by the MPS $|\psi\rangle$ is defined as $\rho = |\psi\rangle\langle\psi|$. To describe only a part of the system, we need to calculate the reduced density matrix. Let I be a set of sites and $\sigma_s = \{\sigma_{k\in I}\}$ a fused index for their local states. Tracing out all other sites with combined index $\sigma_b = \{\sigma_{k\notin I}\}$, we obtain

$$\rho_I = \sum_{\sigma_1 \ldots \sigma_N \sigma'_1 \ldots \sigma'_N} \delta_{\sigma_b \sigma'_b} (A^{[\sigma'_1]} \ldots A^{[\sigma'_N]})^* (A^{[\sigma_1]} \ldots A^{[\sigma_N]}) |\sigma_s\rangle\langle\sigma'_s|. \tag{A.21}$$

This is a completely general expression, but in the cases where $I = \{k\}$ or $I = \{k, k'\}$ it reduces to (see figure A.9)

$$\rho_{\{k\}} = P^{[L_k]} (A^{[\sigma_k]} \otimes A^{[\sigma'_k]^*}) P^{[R_k]} |\sigma_k\rangle\langle\sigma'_k|, \tag{A.22}$$

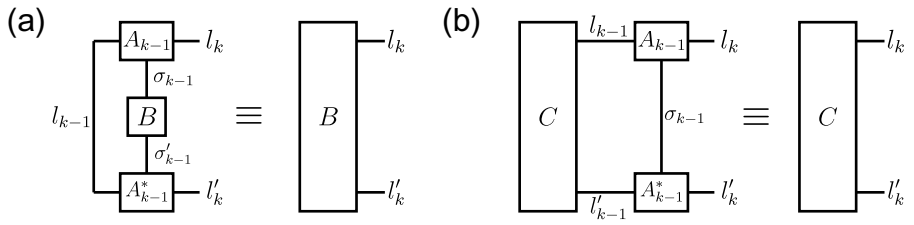

Figure A.10. The k-left representation of (a) the operator B, obtained from its $(k-1)$-local-representation, and (b) the operator C, obtained from its $(k-1)$-left-representation.

$$B_{\sigma'_i\sigma_i} \longrightarrow B_{l'_{i+1}l_{i+1}} \longrightarrow B_{l'_{i+2}l_{i+2}} \longrightarrow \ldots \longrightarrow B_{l'_k l_k}$$

Figure A.11. Iterative calculation of the k-left-description of an operator B, given in the i-local-description, by (A.24) and (A.25) for any $k > i$.

$$\rho_{\{kk'\}} = P^{[L_k]}(A^{[\sigma_k]} \otimes A^{[\sigma'_k]^*})P^{[kk']}(A^{[\sigma_{k'}]} \otimes A^{[\sigma'_{k'}]^*})P^{[R_{k'}]}|\sigma_k\rangle|\sigma_{k'}\rangle\langle\sigma'_k|\langle\sigma'_{k'}|. \tag{A.23}$$

A similar strategy can be used to calculate the density matrices needed for the main text, by contracting out the σ_k's for all sites except those involved in the clusters A, B or $A \cup B$. In fact, (A.23) gives $\hat{\rho}^{A\cup B}$ for two clusters of size 1 at sites k and k'.

A.2.8. Operators in an effective basis. Let k be the current site with orthonormal effective basis sets $|l_k\rangle$ and $|r_k\rangle$. Consider an operator B, which acts on the local basis of site $k-1$ only, with matrix elements $B_{\sigma'_{k-1}\sigma_{k-1}} = \langle\sigma'_{k-1}|B|\sigma_{k-1}\rangle$. We call this the $(k-1)$-local-representation of B. To represent B in the effective left basis of site k, called the k-left-representation of B, we use the transformation properties of $A^{[\sigma_{k-1}]}$ (see figure A.10),

$$\begin{aligned}\langle l'_k|B|l_k\rangle &= \left(\langle l'_{k-1}|\langle\sigma'_{k-1}| \sum_{l'_{k-1}\sigma'_{k-1}} A^{[\sigma'_{k-1}]^*}_{l'_{k-1}l'_k}\right) B_{\sigma'_{k-1}\sigma_{k-1}} \left(\sum_{l_{k-1}\sigma_{k-1}} A^{[\sigma_{k-1}]}_{l_{k-1}l_k}|l_{k-1}\rangle|\sigma_{k-1}\rangle\right) \\ &= \sum_{l_{k-1}\sigma'_{k-1}\sigma_{k-1}} A^{[\sigma'_{k-1}]^*}_{l_{k-1}l'_k} A^{[\sigma_{k-1}]}_{l_{k-1}l_k} B_{\sigma'_{k-1}\sigma_{k-1}},\end{aligned} \tag{A.24}$$

where the only condition to derive these results was that site $k-1$ has an orthonormal effective left basis. Similarly, if the $(k-1)$-left-representation of an operator C is known, its k-left-representation can be obtained via (see figure A.10)

$$\langle l'_k|\, C\, |l_k\rangle = \sum_{l_{k-1}l'_{k-1}\sigma_{k-1}} A^{[\sigma_{k-1}]^*}_{l'_{k-1}l'_k} A^{[\sigma_{k-1}]}_{l_{k-1}l_k} C_{l'_{k-1}l_{k-1}}. \tag{A.25}$$

Equations (A.24) and (A.25) can be used iteratively to transcribe the i-local-representation of B into its k-left-representation for any $k > i$ (see figure A.11). This reasoning also applies to the right site of site k and hence it is possible to obtain a description of any local operator on any site.

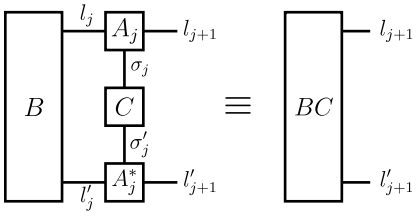

Figure A.12. The $(j+1)$-left-representation of the operators C, given in the j-local-representation, and B, given in the j-left-representation.

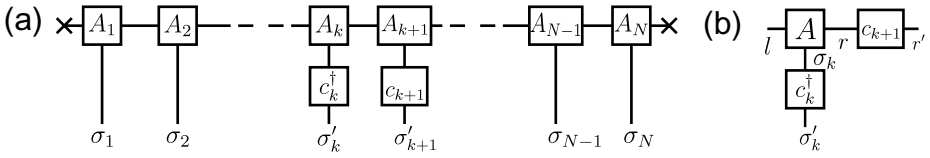

Figure A.13. The nearest-neighbour hopping term $c_k^\dagger c_{k+1}$ acting on $|\psi\rangle$ in (a) the global view and (b) the local view.

To obtain a description of a pair of local operators acting on different sites, we have to transcribe them step by step. Let site k be the current site with orthonormal effective basis sets and B and C two operators acting locally on sites i and j, respectively ($i < j < k$). Firstly, we obtain the j-left-representation of B, namely $B_{l'_j l_j}$, as described above. Then both operators are transformed together into the $(j+1)$-left-representation (see figure A.12),

$$\left\langle l'_{j+1}\right| (BC) \left|l_{j+1}\right\rangle = \sum_{l_j l'_j \sigma_j \sigma'_j} A^{[\sigma'_j]\ *}_{l'_j l'_{j+1}} A^{[\sigma_j]}_{l_j l_{j+1}} B_{l'_j l_j} C_{\sigma'_j \sigma_j}, \tag{A.26}$$

which in turn can be transformed iteratively into the desired k-left-representation of the operators B and C.

A.2.9. Local operators acting on $|\psi\rangle$. Any combination of operators can be calculated directly in the global view or in the local view via the effective descriptions introduced in the previous section.

Global view. The operators, known in the local basis of the site they are acting on, are contracted directly with the corresponding A-matrix. For example, the formula for a nearest-neighbour hopping term $c_k^\dagger c_{k+1}$ (see figure A.13) reads as

$$c_k^\dagger c_{k+1}|\psi\rangle = \sum_{\sigma_1 \ldots \sigma_N} \left(\sum_{\sigma'_k} (c_k^\dagger)_{\sigma'_k \sigma_k} \right) \left(\sum_{\sigma'_{k+1}} (c_{k+1})_{\sigma'_{k+1} \sigma_{k+1}} \right) (A^{[\sigma_1]} \ldots A^{[\sigma_N]})$$
$$\times |\sigma_1\rangle \ldots |\sigma_{k-1}\rangle |\sigma'_k\rangle |\sigma'_{k+1}\rangle |\sigma_{k+2}\rangle \ldots |\sigma_N\rangle. \tag{A.27}$$

Local view. Let k be the current site with orthonormal effective basis sets. If we want to evaluate operators acting on other sites than the current site k, we need an effective description

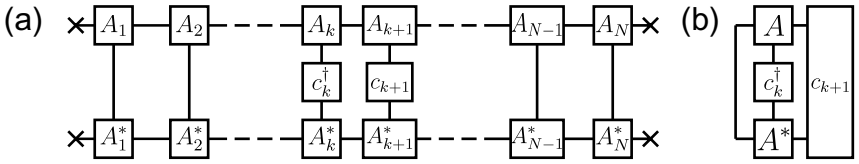

Figure A.14. The expectation value of the nearest-neighbour hopping $c_k^\dagger c_{k+1}$ in (a) the global view and (b) the local view.

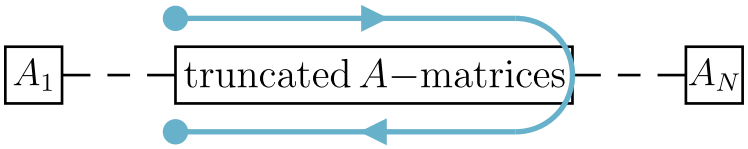

Figure A.15. One complete sweep.

of these operators in one of the effective basis sets of site k to contract these operators with the A-matrix of the current site. For example, to calculate the action of the nearest-neighbour hopping term $c_k^\dagger c_{k+1}$ on $|\psi\rangle = A_{lr}^{[\sigma_k]}|l\rangle|\sigma_k\rangle|r\rangle$, we need $(c_k^\dagger)_{\sigma_k'\sigma_k}$ and $(c_{k+1})_{r'r}$ to obtain (see figure A.13)

$$c_k^\dagger c_{k+1}|\psi\rangle = \sum_{r\sigma_k}\left(\sum_{\sigma_k'}\left(c_k^\dagger\right)_{\sigma_k'\sigma_k}\right)\left(\sum_{r'}(c_{k+1})_{r'r}\right)A_{lr}^{[\sigma_k]}|l\rangle|\sigma_k'\rangle|r'\rangle. \tag{A.28}$$

A.2.10. Expectation values. Expectation values are merely the scalar product between the state with itself including the action of an operator and can be easily worked out in both the global view and the local view (see figure A.14). Since both methods are equivalent, the local variant is much more efficient as it involves many fewer matrix multiplications. However, it requires careful orthonormalization of the remainder of the A-matrices. The iterative scheme, introduced in section A.3, allows for that and works in the local picture.

A.3. Variational optimization scheme

The basic techniques introduced in the previous sections are the building blocks for DMRG sweeps, an iterative scheme to determine the ground state in the usual DMRG sense. This scheme starts at some site as current site, for example the first site where truncation occurs, and minimizes the energy of $|\psi\rangle$ with respect to that site. Afterwards the current site is shifted to the next site, and the energy of $|\psi\rangle$ with respect to that site is minimized. This is repeated until the last site where truncation occurs is reached and the direction of the switches is reversed. When the starting site is reached again, one *sweep* has been finished (see figure A.15). These sweeps are repeated until $|\psi\rangle$ converges.

A.3.1. Energy minimization of the current site. In order to find the ground state of the system we have to minimize the energy $E = \langle\psi|H|\psi\rangle$ of the matrix product state $|\psi\rangle$ with the constraint that the norm of $|\psi\rangle$ must not change. Introducing λ as Lagrange multiplier to ensure

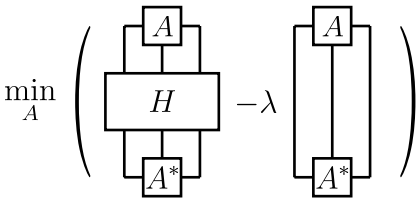

Figure A.16. The minimization problem expressed in the current site.

proper normalization, we arrive at the problem of determining

$$\min_{|\psi\rangle} \left(\langle\psi|\, H\, |\psi\rangle - \lambda \langle\psi|\psi\rangle \right). \tag{A.29}$$

In the sweeping procedure introduced above, the current site is changed from one site to the next and the energy is minimized in each local description. Thus, we need (A.29) in terms of the parameters of the current site. Let us describe how to do this for the case of one-site DMRG, where the A-matrices are optimized one site at a time. (The procedure for two-site DMRG is entirely analogous, except that it involves combining A-matrices of two neighbouring sites by fusing their indices to obtain a combined two-site A-matrix; see section A.2.5.) Inserting (A.1) into (A.29) yields (see figure A.16)

$$\min_{A^{[\sigma]}} \left(\sum_{lr\sigma l'r'\sigma'} A^{[\sigma']*}_{l'r'} H_{l'r'\sigma' lr\sigma} A^{[\sigma]}_{lr} - \lambda \sum_{lr\sigma} A^{[\sigma]*}_{lr} A^{[\sigma]}_{lr} \right), \tag{A.30}$$

where $H_{l'r'\sigma' lr\sigma} = \langle l'|\langle\sigma'|\langle r'|H|l\rangle|\sigma\rangle|r\rangle$ is the Hamiltonian expressed in the two orthonormal effective basis sets and the local basis of the current site.

The multidimensional minimization problem (A.29) has been transformed to a local minimization problem where one A-matrix (or two) is optimized at a time and all others are kept constant. Such a procedure could, in principle, cause the system to get stuck in a local minimum in energy, but experience shows that the procedure works well [5], especially in the presence of a gap.

To obtain a solution for (A.30), we differentiate the equation with respect to $A^{[\sigma']*}_{l'r'}$ (this is possible because the Hilbert space has a Hermitian scalar product) and obtain

$$0 = \sum_{l'r'\sigma'} H_{l'r'\sigma' lr\sigma} A^{[\sigma]}_{lr} - \lambda A^{[\sigma']}_{l'r'}. \tag{A.31}$$

The matrix elements $H_{l'r'\sigma' lr\sigma}$ may be calculated easily using the techniques introduced in section A.2 (see section A.3.2 for details). Changing to matrix notation and replacing λ with E_0 in anticipation of its interpretation as an energy, we obtain an eigenvalue equation:

$$H A^{[\sigma]}_{lr} |l\rangle\, |\sigma\rangle\, |r\rangle = E_0 A^{[\sigma]}_{lr} |l\rangle\, |\sigma\rangle\, |r\rangle\,. \tag{A.32}$$

The minimization problem reduces to a local eigenvalue problem, which can be solved by standard techniques. The full Hilbert space of the current site has dimension dD^2 and may become large, but it is not necessary to determine the full spectrum of H, since we are interested only in the ground state. The Lanczos algorithm is an effective algorithm to achieve exactly

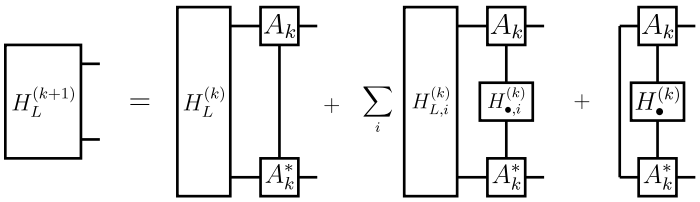

Figure A.17. Iterative calculation of the operator $H_L^{(k+1)}$. The sum over i indicates that $H_{L\bullet}^{(k)}$ has the form $\sum_i H_{L,i}^{(k)} \otimes H_{\bullet,i}^{(k)}$, where $H_{L,i}^{(k)}$ acts only on sites $k' < k$ and $H_{i,\bullet}^{(k)}$ acts only on site k. The calculation of $H_R^{(k-1)}$ works analogously.

that. The advantage of this algorithm is that we only have to compute $H|\psi\rangle$, which saves much effort. The Lanczos algorithm produces as output the ground state eigenvalue and eigenvector. The latter gives the desired optimized version of the matrix A_{lr}^{σ}, which then has to be rewritten (with or without Hilbert space truncation, as needed) into a form that satisfies the orthonormality requirements of the left and right basis sets, as described in section A.2.4.

A.3.2. Sweeping details. Before the actual sweeping may be started we have to set up an initial state, prepare a current site with orthonormal effective basis sets and calculate effective descriptions of operators that are part of the Hamiltonian. After this initialization we may determine the ground state with respect to this current site and shift the current site to the next site. That current site again has orthonormal effective basis sets due to the switching procedure introduced in section A.2.4, but we also need effective representations of the operators acting in the Hamiltonian. At this step the structure of the MPS saves much effort, as most of the needed representations are already calculated.

Structure of the Hamiltonian terms. The Hamiltonian $H_{l'r'\sigma'lr\sigma}$, acting in the space spanned by the states $|l\rangle$, $|\sigma\rangle$ and $|r\rangle$, breaks up into several terms:

$$\begin{aligned} H_{l'r'\sigma'lr\sigma} = {} & \mathbb{1}_{l'l} \otimes (H_\bullet)_{\sigma'\sigma} \otimes \mathbb{1}_{r'r} + (H_L)_{l'l} \otimes \mathbb{1}_{\sigma'\sigma} \otimes \mathbb{1}_{r'r} + \mathbb{1}_{l'l} \otimes \mathbb{1}_{\sigma'\sigma} \otimes (H_R)_{r'r} \\ & + (H_{L\bullet})_{l'l\sigma'\sigma} \otimes \mathbb{1}_{r'r} + \mathbb{1}_{l'l} \otimes (H_{\bullet R})_{r'r\sigma'\sigma} + (H_{L\bullet R})_{l'lr'r\sigma'\sigma}\,, \end{aligned} \tag{A.33}$$

where the indices denote on which parts of the system the respective term acts on (L and R indicate left and right of the current site, respectively, and $\bullet$ indicates action on the current site). Of course, the six terms of (A.33) depend on the current site k: $H_\bullet^{(k)}$, $H_L^{(k)}$, $H_R^{(k)}$, $H_{L\bullet}^{(k)}$, $H_{\bullet R}^{(k)}$ and $H_{L\bullet R}^{(k)}$. The terms $(H_L)_{l'l}$ and $(H_R)_{r'r}$ contain all terms that involve only sites $k' < k$ and $k' > k$, respectively. The iterative structure of the method directly yields the following equalities:

$$H_L^{(k+1)} = H_L^{(k)} + H_{L\bullet}^{(k)} + H_\bullet^{(k)}, \tag{A.34}$$

$$H_R^{(k-1)} = H_\bullet^{(k)} + H_{\bullet R}^{(k)} + H_R^{(k)}, \tag{A.35}$$

where the terms on the rhs are meant to be expressed in the effective basis of the operator on the lhs (see figure A.17).

Initialization. First of all we need an initial MPS, which is most conveniently chosen to consist of identity transformations at the ends of the chain (see section A.2.3) and random A-matrices for the rest of the chain. We take the first site where Hilbert space truncation is applied as current site k and obtain an orthonormal effective right basis (the effective left basis is already orthonormal) using the orthonormalization procedure introduced in section A.2.4 starting from site N. Additionally, it is convenient, while dealing with site N, to calculate and *store* the operator $H_R^{(N-1)}$ (see equation (A.35)) and the effective description of all operators of site N that contribute to $H_{\bullet R}^{(k)}$ and $H_{L\bullet R}^{(k)}$ in the effective right basis of site $N-1$ (see section A.2.8). This ensures, when the sweeping procedure reaches site $N-1$, that all necessary operators are already calculated. This is repeated from site N down to site $k+1$ and similarly for the sites $k' < k$ in the other direction. The result of these initialization steps is that we have a current site k with orthonormal effective basis sets, effective descriptions of the Hamiltonian terms $H_L^{(k)}$ and $H_R^{(k)}$ and effective descriptions of all operators contributing to $H_{L\bullet}^{(k)}$, $H_{\bullet R}^{(k)}$ and $H_{L\bullet R}^{(k)}$. Moreover, with an appropriate extension to the switching procedure of section A.2.4, all effective descriptions for other current sites are available for use when needed in future sweeping steps.

Extended switching procedure. The switching procedure of section A.2.4 is applied as before. Additionally, depending on the direction of the switch, $H_L^{(k+1)}$ or $H_R^{(k-1)}$ are calculated and stored as well as the operators needed for the Hamiltonian (A.33). This extended switching ensures that for the new current site all required operators are calculated if they had been for the old current site.

Complete ground state calculation. The methods introduced above make the procedure for determining the ground state very efficient as the global problem is mapped onto many local problems involving only a few terms to calculate. The iterative structure of the MPSs and the effective Hamiltonian terms strongly increase the efficiency. A full ground state calculation consists of:

(i) Initialization as described above.

(ii) Full sweeps from site K to site K' and back to site K, with sites K and K' being the first and last sites where the effective Hilbert spaces are truncated.

(iii) After each sweep i the overlap $\langle\psi_{i-1}|\psi_i\rangle$ between the state before and after the sweep is calculated. If the MPS does not change any more, stop the sweeping. A criterion, for example, for when to stop would be to require that

$$\frac{|\langle\psi_{i-1}|\psi_i\rangle - \langle\psi_{i-2}|\psi_{i-1}\rangle|}{|\langle\psi_{i-1}|\psi_i\rangle|} \leqslant \epsilon, \tag{A.36}$$

where ϵ is a small control parameter, typically of order 10^{-10}.

Numerical costs. The step with the most impact on the numerical costs of the algorithm is the calculation of $H|\psi\rangle$ in the Lanczos method. This method is an iterative scheme using several *Lanczos steps*, of which usually less than 100 are needed for one ground state calculation. Each Lanczos step calculates $H|\psi\rangle$ exactly once. This calculation basically consists of elementary matrix multiplications, see section A.5.3 for details of the numerical costs of such calculations.

All of the six terms introduced in (A.33) are not equally time consuming. Most of them contain identity maps that do not need to be carried out and thus the term $H_{L\bullet R}$ is the most time consuming, requiring operations of order $\mathcal{O}(dD^2(2D+d))$. The total numerical cost for the minimization process is

$$C = N_{\text{Sweep}} \times 2N \times N_{\text{Lanczos}} \times (dD^2(2D+d)), \tag{A.37}$$

where N_{Sweep} is the number of sweeps, N the chain length and N_{Lanczos} the number of Lanczos steps. In practice the cutoff dimension is significantly higher than the local Hilbert space dimension d and thus (A.37) is nearly linear in d.

A.4. Abelian symmetries

MPSs can be easily adapted to properly account for conserved quantum numbers, representing the global symmetries of the Hamiltonian. We will limit ourselves to Abelian symmetries, meaning that the irreducible representation of the symmetry group is Abelian, as these are easily implemented, which is not necessarily the case for non-Abelian symmetries [36].

An Abelian symmetry allows a quantum number Q to be attached to every state. The property that the symmetry is Abelian manifests itself in that this quantum number is strictly additive. For two states $|Q_1\rangle$ and $|Q_2\rangle$, the quantum number of the direct product of these two states is given by $|Q_1\rangle \otimes |Q_2\rangle = |Q_1 + Q_2\rangle$. For example, if the Hamiltonian commutes with the number operator for the full system, the quantum number Q could represent particle number.

For MPSs, the introduction of Abelian symmetries has the consequence that the A-matrix $A^{[\sigma]}_{lr}$ may be written as $(A^{Q_\sigma}_{Q_l Q_r})^{\gamma_\sigma}_{\alpha_l \beta_r}$. Here Q_σ, Q_l and Q_r are the quantum numbers attached to the local, left effective and right effective basis, respectively. The index α_l distinguishes different states $|Q_l, \alpha_l\rangle$ characterized by the same quantum number Q_l, and similarly for $|Q_r, \beta_r\rangle$ and $|Q_\sigma, \gamma_\sigma\rangle$. If A describes, for example, the mapping of the $|l\rangle$-basis of the left block together with the local basis to a combined (truncated) $|r\rangle$-basis, then the only nonzero blocks of the A-matrix are those for which $Q_\sigma + Q_l = Q_r$. For the current site, the total symmetry Q_{tot} of the full quantum many-body state manifests itself in that the corresponding A-matrix fulfills $Q_l + Q_r + Q_\sigma = Q_{\text{tot}}$.

For the handling of MPSs, quantum numbers imply a significant amount of bookkeeping, i.e. for every coefficient block we have to store its quantum number. The benefit is that we can deal with large effective state spaces at a reasonable numerical cost. The Lanczos algorithm, in particular, takes advantage of the block structure.

Of course, the treatment of Abelian symmetries is generic and not limited to only one symmetry. We may incorporate as many symmetries as exist for a given Hamiltonian, by writing Q as a vector of the corresponding quantum numbers.

A.5. Additional details

A.5.1. Derivation of the orthonormality condition. The orthonormality condition (A.7) is easily derived by induction. The starting point is condition (A.6) and we confine ourselves to the derivation for the left basis. The derivation for the right basis is analogous.

The induction argument can be initialized with site $k = 1$ because its effective left basis is already orthonormal as it consists only of the vacuum state. Now, consider the case that site k has an orthonormal effective left basis and construct the condition for site $k+1$ to have an

orthonormal effective left basis:

$$\begin{aligned}\langle l'_{k+1}|l_{k+1}\rangle &= \left(\sum_{l'_k\sigma'_k}\langle l'_k|\langle\sigma'_k|\, A^{[\sigma'_k]\,*}_{l'_k l'_{k+1}}\right)\left(\sum_{l_k\sigma_k} A^{[\sigma_k]}_{l_k l_{k+1}}\,|l_k\rangle\,|\sigma_k\rangle\right)\\ &= \sum_{l'_k l_k \sigma'_k \sigma_k} A^{[\sigma'_k]\,*}_{l'_k l'_{k+1}} A^{[\sigma_k]}_{l_k l_{k+1}} \underbrace{\langle l'_k|l_k\rangle}_{\delta_{l'_k l_k}} \underbrace{\langle\sigma'_k|\sigma_k\rangle}_{\delta_{\sigma'_k\sigma_k}} = \sum_{l_k\sigma_k} A^{[\sigma_k]\,*}_{l_k l'_{k+1}} A^{[\sigma_k]}_{l_k l_{k+1}}\\ &= \left(\sum_{\sigma_k} A^{[\sigma_k]^\dagger} A^{[\sigma_k]}\right)_{l'_{k+1} l_{k+1}}. \end{aligned} \tag{A.38}$$

Condition (A.7) follows with $\langle l'_{k+1}|l_{k+1}\rangle \stackrel{!}{=} \delta_{l'_{k+1}l_{k+1}}$.

A.5.2. SVD. The SVD can be seen as a generalization of the spectral theorem, i.e. of the eigenvalue decomposition. It is valid for any real or complex $m \times n$ rectangular matrix. Let M be such a matrix; then it can be written in an SVD

$$M = USV^\dagger, \tag{A.39}$$

where U is an $m \times m$ unitary matrix, S is an $m \times n$ matrix with real, non-negative entries on the diagonal and with zeros off the diagonal and V is an $n \times n$ unitary matrix. The numbers on the diagonal of S are called *singular values*, and there are $p = \min(n, m)$ of them. The singular values are unique, but U and V are not, in general. It is convenient to truncate and reorder these matrices in such a fashion that their dimensions are $m \times p$ for U, $p \times p$ for S (with the singular values ordered in a non-increasing fashion) and $n \times p$ for V (i.e. $p \times n$ for $V^\dagger$). A consequence of this truncation is that U or V is no longer quadratic and unitarity is not defined for such matrices. This property is replaced by *column unitarity* (orthonormal columns) of U and *row unitarity* (orthonormal rows) for $V^\dagger$—no matter which one is no longer quadratic. In this paper, all SVDs are understood to be ordered in this fashion.

A.5.3. Numerical costs of index contractions. The numerical costs of matrix multiplications and index contractions of multi-index objects depend on the dimension of both the resulting object and of the contracted indices. In the case of matrix multiplications this is quite simple. Consider an $n \times m$ matrix M_1 multiplied by an $m \times p$ matrix M_2. The result is an $n \times p$ matrix M:

$$M_{ij} = \sum_{k=1}^{m} (M_1)_{ik}\,(M_2)_{kj}\,. \tag{A.40}$$

Evidently, each of the $n * p$ matrix elements M_{ij} requires a sum over m products of the form $(M_1)_{ik}(M_2)_{kj}$. Thus the process for calculating $M_1 M_2$ is of order $\mathcal{O}(nmp)$.

The numerical costs of multi-index objects are obtained analogously. Consider two multi-index objects, M_1 with indices $i_1, \ldots, i_n$ and dimensions $p_1 \times \cdots \times p_n$ and M_2 with indices $j_1, \ldots, j_m$ and dimensions $q_1 \times \cdots \times q_m$. If we contract the indices i_1 and i_2 of M_1 with the indices j_1 and j_2 of M_2 (assuming that $p_1 = q_1$ and $p_2 = q_2$), we obtain the multi-index object M:

$$M_{i_3 \ldots i_n j_3 \ldots j_m} = \sum_{k=1}^{p_1}\sum_{l=1}^{p_2} (M_1)_{kli_3\ldots i_n}\,(M_2)_{klj_3\ldots j_m}\,. \tag{A.41}$$

Thus, for every entry of M, p_1 times p_2 multiplications have to be done, so that the process is of order $\mathcal{O}((p_3 \ldots p_n)(p_1 p_2)(q_3 \ldots q_m))$.

References

[1] Cheong S A and Henley C L 2009 *Phys. Rev.* B **79** 212402
[2] Cheong S A and Henley C L 2009 *Phys. Rev.* B **80** 165124
[3] White S R 1992 *Phys. Rev. Lett.* **69** 2863–6
[4] White S R 1993 *Phys. Rev.* B **48** 10345–56
[5] Schollwöck U 2005 *Rev. Mod. Phys.* **77** 259–315
[6] Verstraete F, Porras D and Cirac J I 2004 *Phys. Rev. Lett.* **93** 227205
[7] Wilson K G 1975 *Rev. Mod. Phys.* **47** 773–840
[8] Vekić M and White S R 1993 *Phys. Rev. Lett.* **71** 4283–6
[9] Andersson M, Boman M and Östlund S 1999 *Phys. Rev.* B **59** 10493–503
[10] Efetov K B and Larkin A I 1976 *Sov. Phys. JETP* **42** 390–6
[11] Micnas R, Ranninger J and Robaszkiewicz S 1988 *J. Phys. Colloq.* **49** C8-2221–6
[12] Furukawa S, Pasquier V and Shiraishi J 2009 *Phys. Rev. Lett.* **102** 170602
[13] Vidal G 2004 *Phys. Rev. Lett.* **93** 040502
[14] White S R and Feiguin A E 2004 *Phys. Rev. Lett.* **93** 076401
[15] Daley A J, Kollath C, Schollwöck U and Vidal G 2004 *J. Stat. Mech.* P04005
[16] García-Ripoll J J 2006 *New J. Phys.* **8** 305
[17] Affleck I, Kennedy T, Lieb E H and Tasaki H 1987 *Phys. Rev. Lett.* **59** 799
[18] Klümper A, Schadschneider A and Zittartz J 1991 *J. Physique* A **24** L955
[19] Fannes M, Nachtergaele B and Werner R F 1992 *Commun. Math. Phys.* **144** 443–90
[20] Klümper A, Schadschneider A and Zittartz J 1992 *Z. Phys.* B **87** 281
[21] Derrida B, Evans M R, Hakim V and Pasquier V 1993 *J. Physique* A **26** 1493
[22] Rommer S and Östlund S 1997 *Phys. Rev.* B **55** 2164
[23] Östlund S and Rommer S 1995 *Phys. Rev. Lett.* **75** 3537–40
[24] Martín-Delgado M A and Sierra G 1996 *Int. J. Mod. Phys.* A **11** 3145
[25] Dukelsky J, Martin-Delgado M A, Nishino T and Sierra G 1998 *Europhys. Lett.* **43** 457–62
[26] Takasaki H, Hikihara T and Nishino T 1999 *J. Phys. Soc. Japan* **68** 1537–40
[27] McCulloch I P 2007 *J. Stat. Mech.* **2007** P10014
[28] Chung M-C and Peschel I 2001 *Phys. Rev.* B **64** 064412
[29] Vidal G, Latorre J I, Rico E and Kitaev A 2003 *Phys. Rev. Lett.* **90** 227902
[30] Schuch N, Wolf M M, Verstraete F and Cirac J I 2008 *Phys. Rev. Lett.* **100** 040501
[31] Korepin V E 2004 *Phys. Rev. Lett.* **92** 096402
[32] Verstraete F, Garcia-Ripoll J J and Cirac J I 2004 *Phys. Rev. Lett.* **93** 207204
[33] Feiguin A E and White S R 2005 *Phys. Rev.* B **72** 220401
[34] Jordan P and Wigner E 1928 *Z. Phys.* **47** 631–51
[35] Verstraete F and Cirac J I 2006 *Phys. Rev.* B **73** 094423
[36] McCulloch I P and Gulácsi M 2002 *Europhys. Lett.* **57** 852–8